An explicit coupled MPM formulation to simulate penetration problems in soils using quadrilateral elements

Martinelli, Mario; Galavi, Vahid

Important note
To cite this publication, please use the final published version (if applicable).
Please check the document version above.

An explicit coupled MPM formulation to simulate penetration problems in soils using quadrilateral elements

Mario Martinelli [a,b,*], Vahid Galavi [a]

[a] *Geo-Engineering Unit, Deltares, Delft, the Netherlands*
[b] *Faculty Civil Engineering & Geosciences, TU Delft, the Netherlands*

ARTICLE INFO

ABSTRACT

This paper describes an MPM formulation using linear quadrilateral elements suitable for soil-structure-interaction problems. The volumetric locking and stress-oscillations are mitigated using a reduced integration technique and the Gauss integration scheme, respectively. The formulation can be used with both structured and unstructured computational meshes. In addition, an improved calculation scheme is proposed to obtain accurate contact reaction forces, especially for contacts between non-porous structures and soils with high liquid pressures. The formulation is validated by simulating a wide range of applications such as a water dam break, 1D large-strain consolidation, and the bearing capacity of a strip footing. Finally, the installation of a cone penetrometer in a centrifuge is successfully simulated in soft soils and compared with the experimental data for the entire range of drainage conditions.

1. Introduction

The simulation of objects penetrating the soil has always been a challenging topic in computational geomechanics. This is mainly due to the numerical difficulties caused by large deformations developed near the penetrating object, and describing the soil behavior over the full strain range (from small to very large).

Several methods have been proposed for the large deformation analysis in the last three decades, such as the Discrete Element Method (DEM) (e.g. Arroyo et al., 2011), the Particle Finite Element Method (PFEM) (e.g. Monforte et al., 2017; Monforte et al., 2018), the Arbitrary Lagrangian-Eulerian method (ALE) (e.g. van den Berg, 1994; Tolooiyan and Gavin, 2011; Fan et al., 2018), the Smoothed Particle Hydrodynamics (SPH) (e.g. Kulak and Bojanowski, 2011), the Coupled Eulerian-Lagrangian Method (CEL) (e.g. Fallah et al., 2016; Staubach et al. 2021) and the Material Point Method (MPM) (e.g. Beuth and Vermeer, 2013; Ceccato et al., 2016; Martinelli and Galavi, 2021).

MPM is gaining attention for the simulation of various installation techniques because of its flexibility. The standard Cone Penetration Tests (CPT) (e.g. Beuth, 2012; Ceccato et al., 2016; Ceccato et al., 2017; Martinelli and Galavi, 2021), jacked piles (e.g. Phuong et al. 2016), and suction-piles (e.g. Martinelli et al. 2020; Stapelfeldt et al., 2021) are some applications of MPM to quasi-static problems, while free-fall penetrometers (e.g. Zambrano and Yerro, 2020), impact-driven piles (e.g. Al-Kafaji, 2013; Hamad, 2016; Moormann et al., 2017; Galavi et al., 2019) and vibro-driven piles (e.g. Galavi et al., 2017) are some successful dynamic problems in which MPM has been used. It is worth mentioning that significant contributions have been made to this field of research by the Anura3D Research Community (www.anura3d.com) by developing the open-source Anura3D code for MPM calculations.

The Anura3D community has widely adopted the linear 3-node triangular element in 2D, and similarly the linear 4-node tetrahedral element in 3D, to simulate large deformation problems (e.g. Beuth, 2012; Al-Kafaji, 2013). It is well known that such low-order elements suffer from volumetric locking. To mitigate this problem, a nodal mixed discretization method - proposed by Stolle et al. (2010) in MPM and inspired by Detournay and Dzik (2006) – is currently being used in Anura3D. This consists of a nodal averaging of the increments of volumetric strains (Beuth, 2012). The method of Stolle et al. (2010) was originally proposed for elastic or elastoplastic materials without considering the volume change caused by plastic shearing. This implies that the volumetric response must be similar in adjacent elements. Therefore, by applying the nodal averaging method in geotechnical applications, in which usually advanced constitutive models are used, the computational mesh should be fine enough to have a smooth transition of volumetric strains and soil response between adjacent elements.

It is widely known that the original material point method (Sulsky et al., 1994) suffers from stress oscillations induced by the movement of the material points through the computational mesh. This is mainly attributed to the use of piecewise basis (shape) functions, which have discontinuous gradients (e.g. Andersen and Andersen, 2009; Stefen et al., 2008; Zhang et al., 2011). Hence, several techniques have been proposed to ensure continuity in the gradient of basis functions at the boundaries between the elements, such as GIMP (Bardenhagen and Kober, 2004), CPDI (Sadeghirad et al., 2011), B-spline MPM (Tielen, 2016; Gan et al., 2018) and DDMP (Zhang et al., 2011).

In Anura3D, the stress-oscillations are mitigated using the so-called Gauss integration method (Beuth, 2012). This method, in contrast to the standard material point integration, uses a fixed number of integration points in an optimal location to achieve the highest accuracy (Beuth and Vermeer, 2013). However, this technique was developed for linear elements with a single Gauss point, where stresses and strains are assumed constant over the element.

This paper provides an alternative formulation for 2D problems based on the 4-node quadrilateral element, for which Gauss integration is used to mitigate the stress-oscillations and the element locking by a reduced-integration. This technique avoids sharing of volumetric strains between elements, which occurs if the nodal averaging technique is applied. Instead, the well-known B-bar method is adopted (Hughes, 2000), in which the deviatoric strains are calculated in all four Gauss points, but only one Gauss point, located in the center of the element, is used for the volumetric strains. This formulation can be used for structured and unstructured computational meshes and can be directly extended to 3D problems using the 8-node hexahedral element.

The effects of the contact formulation and fixities on the numerical scheme are also presented in this paper. An improved computational scheme is proposed to compute accurate reaction forces along contact surfaces, especially between non-porous structures and soils with high liquid pressures (Appendix).

The formulation is validated by simulating a wide range of applications such as a water dam break, 1D large-strain consolidation, and the bearing capacity of a strip footing. Finally, the installation of a cone penetrometer in a centrifuge is successfully simulated in soft soils and compared with the experimental data (Schneider et al., 2007) for the entire range of drainage conditions.

2. Numerical MPM formulations

This section describes the MPM formulations for coupled 2-phase, undrained and drained analyses. It also highlights how the soil-structure interaction is formulated along a contact surface.

2.1. Coupled 2-phase formulation

The primary unknowns of the dynamic MPM formulation are the accelerations of the solid and liquid phases (a_S-a_L) (Jassim et al., 2013). The momentum balance for the liquid phase and the mixture, as well as the mass balance equations and the constitutive relationship, lead to the solution of the system, as written here:

$$\rho_L \boldsymbol{a}_L = \nabla \cdot (p_L \mathbf{I}) + \rho_L \mathbf{b} - \frac{n\mu_L}{\kappa_L}(\boldsymbol{v}_L - \boldsymbol{v}_S) \tag{1}$$

$$(1-n)\rho_S \boldsymbol{a}_S + n\rho_L \boldsymbol{a}_L = \nabla \cdot (\boldsymbol{\sigma}' + p_L \mathbf{I}) + \rho_m \mathbf{b} \tag{2}$$

$$\frac{dn}{dt} = (1-n)(\nabla \cdot \boldsymbol{v}_S) \tag{3}$$

$$\dot{p}_L = \frac{K_L}{n}\left[(1-n)\nabla \cdot \boldsymbol{v}_S + n\nabla \cdot \boldsymbol{v}_L\right] \tag{4}$$

$$\dot{\boldsymbol{\sigma}}' = \boldsymbol{D}\dot{\boldsymbol{\varepsilon}}_s + \Omega\boldsymbol{\sigma}' - \boldsymbol{\sigma}'\Omega - \dot{\varepsilon}_{v,S}\boldsymbol{\sigma}' \tag{5}$$

where n is the porosity; ρ_S and ρ_L are the density of solid grains and pure liquid, respectively; ρ_m is the density of the mixture ($\rho_m = (1-n)\rho_S + n\rho_L$); $\boldsymbol{I}$ is the identity tensor; $\boldsymbol{v}_S$ and $\boldsymbol{v}_L$ are the velocities of the soil and liquid phases, respectively; σ' is the effective stress tensor; K_L is the bulk modulus of the pure liquid, and $\boldsymbol{b}$ is the body force vector. In Eq. (5), the term $\boldsymbol{D}$ is the stiffness matrix; $\dot{\sigma}'$ and $\dot{\varepsilon}_s$ are the stress and strain rate tensors of the solid phase, respectively. Ω is the spin tensor and $\dot{\varepsilon}_{v,S}$ is the volumetric strain increment. Eq. (5) is derived using the Jaumann's stress rate of Kirchhoff stress (objective stress rate), needed to obtain frame-independent results in case of large deformation analyses (Ji et al., 2010; Al-Kafaji, 2013).

It should be noted that Eq. (4) is written based on the assumption that the porosity field is sufficiently smooth over the entire domain of the mixture. As highlighted by Ceccato et al. (2018), this hypothesis is reasonable but may lead to errors when adjacent materials have significantly different porosities.

The contribution of the hydrostatic pressure $\left(p_{hydr}\right)$ can be eliminated from Eqs. (1) and (2) for fully submerged materials, i.e.:

$$\rho_L \boldsymbol{a}_L = \nabla \cdot (\Delta p_L \mathbf{I}) - \frac{n\mu_L}{\kappa_L}(\boldsymbol{v}_L - \boldsymbol{v}_S) \tag{6}$$

$$(1-n)\rho_S \boldsymbol{a}_S + n\rho_L \boldsymbol{a}_L = \nabla \cdot (\boldsymbol{\sigma}' + \Delta p_L \mathbf{I}) + (\rho_m - \rho_L)\mathbf{b} \tag{7}$$

where $\Delta p_L = p_L - p_{hydr}$ is the excess liquid pressure.

2.1.1. Discretized form

For a generic node i of the computational mesh, Eq. (1) is discretized as follows:

$$\overline{M}_{L,i} a_{L,i} = \overline{f}_{L,i}^{ext} - \overline{f}_{L,i}^{int} + \overline{f}_i^{drag} \tag{8}$$

where $\overline{M}_{L,i}$, $\overline{f}_{L,i}^{ext}$, $\overline{f}_{L,i}^{int}$ and $\overline{f}_i^{drag}$ are the nodal values of the liquid mass matrix, external force, internal force and drag force vectors, respectively, summarized as follows:

$$\overline{M}_{L,i} = \sum_{el=1}^{N_{el,i}} \sum_{MP=1}^{N_{MP,el}} N_i(\xi_{MP})\overline{m}_{MP,L} \tag{9}$$

$$\overline{f}_{L,i}^{ext} = \sum_{el=1}^{N_{el,i}} \sum_{MP=1}^{N_{MP,el}} \boldsymbol{N}_i(\xi_{MP})\overline{t}_{MP,L} + \sum_{el=1}^{N_{el,i}} \sum_{MP=1}^{N_{MP,el}} N_i(\xi_{MP})\overline{m}_{MP,L}\boldsymbol{g} \tag{10}$$

$$\overline{f}_{L,i}^{int} = \sum_{el=1}^{N_{el,i}} \sum_{MP=1}^{N_{MP,el}} \boldsymbol{B}_i^T(\xi_{MP})p_{L,MP}\mathbf{I}\Omega_{MP} \tag{11}$$

$$\overline{f}_i^{drag} = \left(\boldsymbol{v}_{S,i} - \boldsymbol{v}_{L,i}\right)\sum_{el=1}^{N_{el,i}} \sum_{MP=1}^{N_{MP,el}} N_i(\xi_{MP})n_{MP}\frac{\mu_{MP}}{\kappa_{MP}}\Omega_{MP} \tag{12}$$

where $N_{el,i}$ is the number of elements around node i; $N_{MP,el}$ is the number of material points in element el; $N_i(\xi_{MP})$ is the value of the shape function calculated at the position of the material point; $\boldsymbol{g}$ is the gravitational vector; κ_{MP} and μ_{MP} are the intrinsic permeability and the dynamic viscosity of the liquid, respectively; $\overline{t}_{MP,L}$, $p_{L,MP}$ and Ω_{MP} are the external load (on the liquid phase), the liquid pressure and the integration weight of the material point, respectively, and $\overline{m}_{MP,L} = \rho_L\Omega_{MP}$ is the liquid mass of the material point.

Eq. (2) is discretized for a generic node i of the computational mesh as:

$$M_{S,i}\boldsymbol{a}_{S,i} + M_{L,i}\boldsymbol{a}_{L,i} = \boldsymbol{f}_i^{ext} - \boldsymbol{f}_i^{int} \tag{13}$$

with:

$$M_{S,i} = \sum_{el=1}^{N_{el,i}} \sum_{MP=1}^{N_{MP,el}} N_i(\xi_{MP}) m_{MP,S} \tag{14}$$

$$M_{L,i} = \sum_{el=1}^{N_{el,i}} \sum_{MP=1}^{N_{MP,el}} N_i(\xi_{MP}) m_{MP,L} \tag{15}$$

$$\boldsymbol{f}_i^{ext} = \sum_{el=1}^{N_{el,i}} \sum_{MP=1}^{N_{MP,el}} N_i(\xi_{MP}) \boldsymbol{t}_{MP} + \sum_{el=1}^{N_{el,i}} \sum_{MP=1}^{N_{MP,el}} N_i(\xi_{MP}) m_{MP} \boldsymbol{g} \tag{16}$$

$$\boldsymbol{f}_i^{int} = \sum_{el=1}^{N_{el,i}} \sum_{MP=1}^{N_{MP,el}} B_i^T(\xi_{MP}) (\boldsymbol{\sigma}_{MP}' + p_{L,MP}\mathbf{I}) \Omega_{MP} \tag{17}$$

where t_{MP} and σ'_{MP} are the (total) external load and the effective stress of the material point, and $m_{MP,L} = n\rho_L\Omega_{MP}$ and $m_{MP,S} = (1-n)\rho_S\Omega_{MP}$ are the liquid and solid masses of the material point, respectively.

2.1.2. Contact formulation

The contact algorithm – originally proposed by Bardenhagen et al. (2000) for frictional contacts and further extended by Al-Kafaji (2013) for adhesive contacts – is used to model separation and sliding between a structure and surrounding soils. The calculated soil velocities are corrected to avoid interpenetration when the following inequality is satisfied:

$$\left(\boldsymbol{v}_{S,i} - \boldsymbol{v}_{structure,i}\right) \cdot \boldsymbol{n}_i > 0 \tag{18}$$

where $\boldsymbol{n}_i$ is the outward unit vector normal to the soil body at node i; $\boldsymbol{v}_{S,i}$ is the velocity of the soil and $\boldsymbol{v}_{structure,i}$ is the velocity of the structure.

The algorithm was extended by Ceccato (2014) to modify the velocity of the liquid for impermeable contact surfaces. The correction was applied to the normal component of the velocity of the liquid phase, $\boldsymbol{v}_{L,i}$, to prevent inflow into the structure and not the outflow. In this paper, the velocity of the liquid phase is corrected to prevent both inflow and outflow, in order to satisfy the following equality:

$$\left(\boldsymbol{v}_{L,i} - \boldsymbol{v}_{structure,i}\right) \cdot \boldsymbol{n}_i = 0 \tag{19}$$

2.1.3. Reaction forces in the coupled formulation

Both fixities (F) and the contact formulation (C) modify the nodal accelerations and nodal velocities in the computational scheme. Thus, it is important to carefully consider how these conditions (i.e. F/C) are treated in the numerical solution of coupled problems, as they can be applied independently to the solid and to the liquid phases.

Eqs. (8) and (13) define the rate of momentum for the solid and liquid phases before applying fixities or contact formulation. Therefore, an additional force term appears in the equations after imposing F/C conditions, indicated as $\boldsymbol{f}^R$, as follows:

$$\overline{M}_{L,i}\boldsymbol{a}_{L,i}\big|_{afterF/C} = \overline{M}_{L,i}\boldsymbol{a}_{L,i} + \overline{\boldsymbol{f}}_{L,i}^R \tag{20}$$

$$M_{S,i}\boldsymbol{a}_{S,i}\big|_{afterF/C} + M_{L,i}\boldsymbol{a}_{L,i}\big|_{afterF/C} = M_{S,i}\boldsymbol{a}_{S,i} + M_{L,i}\boldsymbol{a}_{L,i} + \boldsymbol{f}_i^R \tag{21}$$

where, $\overline{\boldsymbol{f}}_{L,i}^R$ and $\boldsymbol{f}_i^R$ represent nodal reaction force due to F/C, respectively to the liquid phase and to the mixture. If node i appears on the free surface of the soil body, where no fixities and contact is applied, $\overline{\boldsymbol{f}}_{L,i}^R$ includes external loads due to an equivalent liquid pressure ($\widetilde{p}_L$) acting on node i. The corresponding nodal force can be computed as follows:

$$\overline{\boldsymbol{f}}_{L,i}^R = \int_{Area,i} \widetilde{p}_L \mathbf{I} \cdot \boldsymbol{j} ds \tag{22}$$

where $\boldsymbol{j}$ is the outward unit normal vector to the soil body; ds is the area around node i and $\mathbf{I}$ is the identity vector.

The same analogy can be described for the external load due to the equivalent liquid pressure ($\widetilde{p}_L$) and the effective stress ($\widetilde{\boldsymbol{\sigma}}'$) on the surface of the soil body around node i. This force can be determined as:

$$\boldsymbol{f}_i^R = \int_{Area,i} \left(\widetilde{\boldsymbol{\sigma}}' + \widetilde{p}_L\mathbf{I}\right) \cdot \boldsymbol{j} ds = \int_{Area,i} \widetilde{\boldsymbol{\sigma}}' \cdot \boldsymbol{j} ds + \int_{Area,i} \widetilde{p}_L\mathbf{I} \cdot \boldsymbol{j} ds = \boldsymbol{f}_{S,i}^R + \overline{\boldsymbol{f}}_{L,i}^R \tag{23}$$

Thus, there are two forces contributing to $\boldsymbol{f}_i^R$, namely $\boldsymbol{f}_{S,i}^R$ on the solid skeleton and $\overline{\boldsymbol{f}}_{L,i}^R$ on the liquid phase.

The nodal liquid mass $M_{L,i}$ can be approximated for smooth porosity fields as follows:

$$M_{L,i} = n_i\overline{M}_{L,i} \tag{24}$$

where n_i is the nodal value of the soil porosity, computed as:

$$n_i = \frac{\sum_{el=1}^{N_{el,i}} \sum_{MP=1}^{N_{MP,el}} N_i(\xi_{MP}) n_{MP}\Omega_{MP}}{\sum_{el=1}^{N_{el,i}} \sum_{MP=1}^{N_{MP,el}} N_i(\xi_{MP})\Omega_{MP}} \tag{25}$$

By combining Eqs. (20), (21), (23), and Eq. (24), the reaction forces are computed as follows:

$$\overline{\boldsymbol{f}}_{L,i}^R = \overline{M}_{L,i}\left(\boldsymbol{a}_{L,i}\big|_{afterF/C} - \boldsymbol{a}_{L,i}\right) \tag{26}$$

$$\boldsymbol{f}_{S,i}^R = M_{S,i}\left(\boldsymbol{a}_{S,i}\big|_{afterF/C} - \boldsymbol{a}_{S,i}\right) - (1-n_i)\overline{\boldsymbol{f}}_{L,i}^R \tag{27}$$

It should be noted that the term $(1-n_i)\overline{\boldsymbol{f}}_{L,i}^R$ in Eq. is the equivalent reaction forces of the liquid phase due to fixities and contact formulation, which affects the rate of momentum of the solid phase. This term is essential to correctly compute the reaction forces along the contact surface. A verification example is illustrated in the Appendix.

2.1.4. Computational cycle

A single computational cycle of the *modified-Lagrangian* scheme (Sulsky et al. 1994) is described as follows:

1. Compute the nodal porosity (Eq. (25)), assemble the nodal mass, the external force, the internal force and the drag force vectors (Eqs. (9)–(12) and Eqs. (14)–(17));
2. The nodal acceleration of the liquid phase $\boldsymbol{a}_{L,i}^{t+1}$ is determined by solving

$$\boldsymbol{a}_{L,i}^{t+1} = \left(\overline{\boldsymbol{f}}_{L,i}^{ext} - \overline{\boldsymbol{f}}_{L,i}^{int} + \overline{\boldsymbol{f}}_i^{drag}\right)\Big/\overline{M}_{L,i} \tag{28}$$

3. The nodal velocity of the liquid phase $\boldsymbol{v}_{L,i}^{t+1}$ is computed from the nodal acceleration $\boldsymbol{a}_{L,i}^{t+1}$ as follows:

$$\boldsymbol{v}_{L,i}^{t+1} = \boldsymbol{v}_{L,i}^t + \boldsymbol{a}_{L,i}^{t+1}\Delta t \tag{29}$$

4. Contact formulation, fixities and corresponding reaction forces of the liquid phase:
   a. On "impermeable" contact nodes, the corrected velocity $\widehat{\boldsymbol{v}}_{L,i}^{t+1}$ is computed to avoid interpenetration or separation, such that Eq. (19) is satisfied. The acceleration $\boldsymbol{a}_{L,i}^{t+1}\big|_{afterF/C}$ is then updated:

$$\boldsymbol{a}_{L,i}^{t+1}\Big|_{afterF/C} = \left(\widehat{\boldsymbol{v}}_{L,i}^{t+1} - \boldsymbol{v}_{L,i}^t\right)\Big/\Delta t \tag{30}$$

   b. if a fixity is imposed on a degree of freedom at node i, the corresponding $\boldsymbol{a}_{L,i}\big|_{afterF/C}$ is set to zero.
   c. The reaction force $\overline{\boldsymbol{f}}_{L,i}^R$ is then computed as follows:

$$\overline{\boldsymbol{f}}_{L,i}^R = \overline{M}_{L,i}\left(\boldsymbol{a}_{L,i}\big|_{afterF/C} - \boldsymbol{a}_{L,i}\right) \tag{31}$$

5. The nodal acceleration of the solid phase $a_{S,i}^{t+1}$ is determined by solving:

$$a_{S,i}^{t+1} = \left(f_i^{ext} - f_i^{int} + f_{i,0}^{R} - M_{L,i} a_{L,i}^{t+1} \big|_{afterF/C} \right) \big/ M_{S,i} \qquad (32)$$

where $f_{i,0}^{R} = \bar{f}_{L,i}^{R}$ because, at this step, the fixities and contact formulation are only applied to the liquid phase.

6. The nodal velocity of the solid phase $v_{S,i}^{t+1}$ is computed from the nodal acceleration before imposing boundary conditions as follows:

$$v_{S,i}^{t+1} = v_{S,i}^{t} + a_{S,i}^{t+1} \Delta t \qquad (33)$$

7. Fixities, contact formulation and corresponding reaction forces of the solid phase:

    a. The normal velocities are corrected along the contact nodes to avoid interpenetration when Eq. (18) is satisfied. The tangential velocity is adjusted considering the frictional and adhesion contact formulation illustrated in Al-Kafaji (2013). Therefore, the acceleration vector is updated as follows:

$$a_{S,i}^{t+1} \big|_{afterF/C} = \left(\hat{v}_{S,i}^{t+1} - v_{S,i}^{t} \right) \big/ \Delta t \qquad (34)$$

where $\hat{v}_{S,i}^{t+1}$ is the corrected solid velocity vector after contact formulation.

    b. If a fixity is imposed on a degree of freedom at node i, the corresponding $a_{S,i}^{t+1} \big|_{afterF/C}$ is set to zero.

    c. The reaction force $f_{S,i}^{R}$ is then computed as follows:

$$f_{S,i}^{R} = M_{S,i} \left(a_{S,i} \big|_{afterF/C} - a_{S,i} \right) - (1 - n_i) \bar{f}_{L,i}^{R} \qquad (35)$$

8. The total reaction force is then:

$$f_i^{R} = f_{S,i}^{R} + \bar{f}_{L,i}^{R} \qquad (36)$$

9. The velocities of material points are then computed from the nodal accelerations as follows:

$$v_{MP,L}^{t+1} = v_{MP,L}^{t} + \sum_{i=1}^{N_{nodes,el}} N_i(\xi_{MP}^t) a_{L,i}^{t+1} \big|_{afterF/C} \Delta t \qquad (37)$$

$$v_{MP,S}^{t+1} = v_{MP,S}^{t} + \sum_{i=1}^{N_{nodes,el}} N_i(\xi_{MP}^t) a_{S,i}^{t+1} \big|_{afterF/C} \Delta t \qquad (38)$$

10. The nodal velocities are computed as the ratio between the nodal momentum and the nodal mass vectors, as follows:

$$\overline{P}_{i,L}^{t+1} = \sum_{el=1}^{N_{el,i}} \sum_{MP=1}^{N_{MP,el}} N_i(\xi_{MP}^t) \overline{m}_{MP,L} v_{MP,L}^{t+1} \qquad (39)$$

$$P_{i,S}^{t+1} = \sum_{el=1}^{N_{el,i}} \sum_{MP=1}^{N_{MP,el}} N_i(\xi_{MP}^t) m_{MP,S} v_{MP,S}^{t+1} \qquad (40)$$

$$v_{i,L}^{t+1} = \frac{\overline{P}_{i,L}^{t+1}}{\overline{M}_{i,L}}; v_{i,S}^{t+1} = \frac{P_{i,S}^{t+1}}{M_{i,S}} \qquad (41)$$

11. Strain increments are then computed at the location of each material point.

12. Stress is integrated using a constitutive model (Eq. (5)) and the increment of the liquid pressure is calculated using Eq. (4).

13. Porosities n_{MP} are updated using Eq. (3) to recalculate the integration weight of material points as $\Omega_{MP} = m_{MP,S}/(\rho_S(1 - n_{MP}))$.

14. Incremental nodal displacements of the solid phase are updated as follows:

$$\Delta u_{i,S}^{t+1} = \Delta u_{i,S}^{t} + v_{i,S}^{t+1} \Delta t \qquad (42)$$

15. The position of each material point is finally updated using the incremental nodal displacements of the solid phase, which are reset afterwards, as follows:

$$x_{MP}^{t+1} = x_{MP}^{t} + \sum N_i(\xi_{MP}^t) \Delta u_{i,S}^{t+1} \qquad (43)$$

$$\Delta u_{i,S}^{t+1} = 0 \qquad (44)$$

It should be noted that the computational scheme can be converted to the *identical-Lagrangian* scheme by skipping steps (1) and (10). As discussed in Martinelli and Galavi (2021), step (10) is not performed for all contact nodes to avoid spurious stress oscillations and consequently increase the accuracy.

2.2. Single-phase undrained and drained formulation

The mechanical description of the mixture can be simplified in undrained conditions by using accelerations (a_m) and velocities (v_m) of the mixture without the need to describe the solid and the liquid phases separately. It is worth mentioning that the contact formulation is also simplified in that the velocity of the mixture is used, and the contact forces are then calculated as results of total stresses.

The governing equations in undrained conditions are written as follows:

$$\rho_m a_m = \nabla \cdot (\sigma' + p_L \mathbf{I}) + \rho_m \mathbf{b} \qquad (45)$$

$$\frac{dn}{dt} = (1 - n)(\nabla \cdot v_m) \qquad (46)$$

$$\dot{\sigma}' = D \dot{\varepsilon}_m + \Omega \sigma' - \sigma' \Omega - \dot{\varepsilon}_{v,m} \sigma' \qquad (47)$$

$$\dot{p}_L = \frac{K_w}{n} \nabla \cdot v_m \qquad (48)$$

where ρ_m is the density of the mixture, computed as $\rho_m = (1 - n)\rho_S + n\rho_L$.

If the soil is fully underwater, the contribution of the hydrostatic pressure can be removed from Eq. (45), as written in Eq. (7).

In drained conditions, Eqs. (45)–(47) are written in terms of accelerations and velocities of the solid phase. $\dot{p}_L$ is zero and the inertia term is computed as $(1 - n)\rho_S a_S$. In dry conditions, the density of the liquid phase is zero, thus $\rho_m = (1 - n)\rho_S$ in Eqs. (45)–(47).

2.3. Critical time step

The explicit integration scheme, presented in Section 2.1.4, is conditionally stable. The critical time step, defined by the Courant-Friedrichs-Levy (CFL) condition (Courant et al., 1928), is the time increment in which a wave with celerity c travels the smallest element length L_{min}, i.e.:

$$\Delta t_{CFL} = \frac{L_{min}}{c} = \frac{L_{min}}{\sqrt{\hat{E}_{oed}/\rho_m}} \qquad (49)$$

where $\hat{E}_{oed}$ is the undrained constrained modulus of the solid skeleton. For drained simulations, $\hat{E}_{oed}$ is the drained constrained modulus of the

soil skeleton and $\rho_m = (1-n)\rho_S$.

Eq. (49) is found to be insufficient in 2-phase coupled explicit simulations when of the permeability of the soil is low. Mieremet et al. (2016) suggested the following additional permeability-dependent stability criterion:

$$\Delta t_k = \frac{-\rho_L g \Big/ \rho^m k + \sqrt{\left(\rho_L g / \rho^m k\right)^2 + 4\omega^2}}{\omega^2} \tag{50}$$

where $\omega^2 = (4E^{'}/\rho^m)L_{min}^2$, $\rho^m = \rho_m + (1/n - 2)\rho_L$, $E^{'}$ is the drained Young modulus of the solid skeleton and k is the hydraulic conductivity defined as follows:

$$k = \gamma_w \frac{\kappa}{\mu} \tag{51}$$

When the permeability of the soil is high, the following consolidation-dependent criterion might become dominant:

$$\Delta t_{c_v} = \frac{L_{min}^2}{2c_v} \tag{52}$$

$$c_v = \frac{\kappa}{\mu\left(\frac{1}{E^{'}_{oed}} + \frac{n}{K_L}\right)} \tag{53}$$

where $E^{'}_{oed}$ is the drained constrained modulus (oedometric stiffness) of the soil skeleton and K_L is the bulk modulus of the liquid phase.

The critical time step is then determined as the minimum value of the above three criteria:

$$\Delta t_{crit} = min\left(\Delta t_{CFL}, \Delta t_k, \Delta t_{c_v}\right) \tag{54}$$

The criteria do not consider the nonlinearity in the stress–strain relationships. Therefore, to achieve stable solutions in nonlinear calculations, the critical timestep can be reduced by multiplying Δt_{crit} by an additional factor (namely Courant number, Belytschko et al., 2014). The Courant number varies between 0 and 1. Smaller Courant numbers result in smaller time steps, which also improves the accuracy of the numerical results. Throughout this paper, the value of 0.9 is used for all simulations.

2.4. Numerical enhancements of the MPM model

The numerical techniques – used to increase calculation speed, stability, and accuracy of the results – are discussed in this section.

2.4.1. Volumetric locking mitigation techniques

The standard linear 4-noded quadrilateral elements suffer from volumetric locking. To mitigate this problem, the B-bar method is used (Hughes, 2000) in the proposed MPM formulation. In this approach, the internal force and strain increments are calculated using a modified B matrix (named B-bar), where the isotropic components are evaluated at the centre of the element rather than at the local position of each material point. This method prevents volumetric locking without introducing hourglassing deformation modes.

2.4.2. Stress-oscillation mitigation technique

Gauss integration is adopted to mitigate stress oscillation. This technique was originally developed for linear 3-node triangular elements (Beuth, 2012). In this paper, it is extended to 4-node quadrilateral elements. The element is divided into four sub-elements, one for each Gauss point (GP), defined based on the local coordinates. In axisymmetric conditions, the volume of each GP (Ω_{GP}) is computed by multiplying the area of GP by its initial radius (distance between GP and the axis of symmetry).

The effective stress tensor at each of the four GPs is computed by the weighted average of the effective stress tensors of all material points, as follows:

$$\overline{\boldsymbol{\sigma}}^{'}_{GP} = \frac{\sum_{MP=1}^{N_{MP,GP}} \boldsymbol{\sigma}^{'}_{MP} \Omega_{MP}}{\sum_{MP=1}^{N_{MP,GP}} \Omega_{MP}} \tag{55}$$

where Ω_{MP} is the volume of the material point *MP* and $N_{MP,GP}$ is the number of material points located in each sub-element.

Using a similar technique adopted in FLAC (Itasca, 2016), the isotropic part of the effective stress tensor ($\overline{p}^{'}_{GP}$) is averaged over the entire element and the deviatoric part is recalculated accordingly:

$$p^{'}_{el} = \frac{\sum_{GP=1}^{N_{GP}} \overline{p}^{'}_{GP} \Omega_{GP}}{\Omega_{el}} \tag{56}$$

$$\widehat{\overline{\boldsymbol{\sigma}}}^{'}_{GP} = \overline{\boldsymbol{\sigma}}^{'}_{GP} - \left(\frac{1}{3} tr\left(\overline{\boldsymbol{\sigma}}^{'}_{GP}\right) - p^{'}_{el}\right) I \tag{57}$$

The average effective stress tensor ($\widehat{\overline{\boldsymbol{\sigma}}}^{'}_{GP}$) is then assigned back to all material points in the sub-element. When an advanced constitutive model is used, the state variables are averaged over the entire element and reassigned to the material points. The porosity (or void ratio) is also averaged over the element.

Eqs. (55)–(57) are also used for stress averaging in the liquid phase. However, since the stress tensor is isotropic in this case, the element is characterized by only a constant liquid pressure ($p_{L,el}$) after stress averaging.

The internal force vector is then integrated as follows:

$$f_i^{int} = \sum_{el=1}^{N_{el,i}} \sum_{GP=1}^{N_{GP,el}} B_i^T\left(\xi_{GP}\right)\left(\widehat{\overline{\boldsymbol{\sigma}}}^{'}_{GP} + p_{L,el}\mathbf{I}\right)\Omega_{MP} \tag{58}$$

where ξ_{GP} is the local coordinate of the Gauss point in the element and $N_{GP,el}$ is the number of Gauss points in the element.

2.4.3. Mass scaling

To speed-up calculations in explicit integration schemes, time steps can be increased by multiplying the mass matrices by a Mass-Scaling-Factor (MSF), which is larger than 1. This procedure is typically used for quasi-static processes as described in Al-Kafaji (2013).

2.4.4. Numerical damping

The combined damping is used in this formulation (Itasca, 2016). The nodal damping force is calculated as follows:

$$f_{\xi,i}^{damp} = \alpha_{damp}\left|\dot{f}_{\xi,i}\right|\left[sign\left(\dot{f}_{\xi,i}\right) - sign\left(v_{\xi,i}\right)\right]\Big/2 \tag{59}$$

where ξ is the phase (S or L); α_{damp} is the damping factor; $v_{\xi,i}$ is the nodal velocity. The term $\dot{f}_{\xi,i}$ is calculated as follows:

$$\dot{f}_{L,i} = \overline{f}_{L,i}^{ext} - \overline{f}_{L,i}^{int} \tag{60}$$

$$\dot{f}_{S,i} = f_i^{ext} - f_i^{int} - n_i\left(\overline{f}_{L,i}^{ext} - \overline{f}_{L,i}^{int}\right) + (1 - n_i)\overline{f}_{L,i}^{R} \tag{61}$$

As described in Martinelli and Galavi (2021), no damping factor is defined at contact nodes to achieve accurate reaction forces.

3. Validation examples

The proposed MPM formulation is validated by a series of applications. Although the purpose of this paper is primarily the penetration problems in saturated media, some examples are discussed to illustrate the capabilities of the proposed numerical approach in a wider range of applications. A dam break problem is studied first, followed by the consolidation process in saturated media and the bearing capacity of a strip foundation. Finally, the cone penetration test in soft soils is
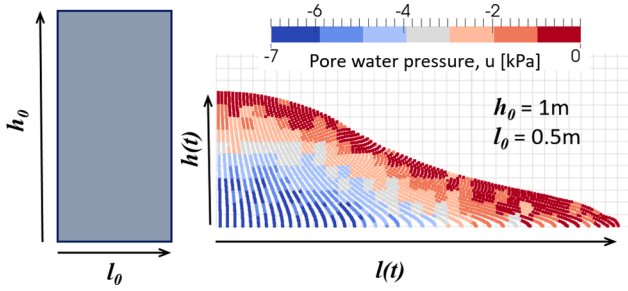
Fig. 1. Dam break problem. Geometry and pore water pressure distribution during the flow at t = 0.4 s.

illustrated including the effect of partially drained conditions.

3.1. Dam break problem

Fig. 1 shows a simplified model of a dam break problem. The model consists of a water column with an initial height, h_0, and an initial length, $l_0 = 0.5$ m. It is initially in equilibrium due to the normal fixities on the lateral and bottom boundaries. At time t = 0, the fixities along the right boundary are removed and the water flows freely under gravity (g = 9.81 m/s^2). The water is modeled as a single-phase material with a density of 1 Mg/m^3 and a bulk modulus of 200 MPa. A structured computational mesh (4-node quadrilateral elements) is used with a uniform element size of 5 cm and 16 material points in each element. Two aspect ratios are considered in this study: $h_0/l_0 = 1$ and $h_0/l_0 = 2$. The pore water pressure distribution is illustrated in Fig. 1 for the case $h_0/l_0 = 2$ at t = 0.4 s. The runout process is described using the following normalized parameters:

$$T = t\sqrt{\frac{h_0 g}{l_0^2}}; H = \frac{h(t)}{h_0}; L = \frac{l(t)}{l_0} \tag{62}$$

The results of the MPM simulations, illustrated in Fig. 2, are in agreement with the benchmark example of Martin and Moyce (1952) and with an independent MPM study of the same example performed by Mast et al. (2012). It can be concluded that the numerical scheme proposed in this paper is able to describe the kinematics of the water flow with a satisfactory pressure field.

3.2. One-dimensional large-strain consolidation

The one-dimensional consolidation problem is a simple example, usually adopted to demonstrate the accuracy of MPM formulations. For example, Spiezia et al. (2015) compared the results of a 1D large-strain consolidation in an implicit Updated Lagrangian FEM with an explicit 2-

phase MPM, and found a satisfactory agreement for the settlement of the column but not for the evolution of pore pressures. Zheng et al. (2021) used the analytical solution of Xie and Leo (2004) and verified their MPM formulation obtaining a good match for both the settlement and pore pressures. The analytical solution of Xie and Leo (2004) is an extension of the one-dimensional large-strain consolidation theory of fully saturated homogeneous clays, derived by Gibson et al. (1967).

In this section, the same example of Zheng et al. (2021) is considered and compared with the analytical solution to verify the presented MPM formulation. The example consists of a weightless elastic soil column with a height of 1 m. The lateral and base boundaries are impermeable and fixed in normal directions. The material properties of the soil are listed in Table 1. A structured background mesh (4-node quadrilateral elements) is used with a uniform element size of 1 cm and 25 material points in each element.

First, a uniformly distributed load of $q_u = 200$ kPa is applied on top of the column under undrained conditions to generate initial pore pressures in the column. Then, the consolidation is simulated using the coupled two-phase material point method. During the consolidation process, water flows out of the ground surface which results in decreasing pore pressure and settlement of the soil column.

The solution of Xie and Leo (2004) was derived assuming the following relationship for hydraulic conductivity as a function of porosity:

$$k = k_0 \left(\frac{1 - n_0}{1 - n}\right)^2 \tag{63}$$

in which k_0 is the initial hydraulic conductivity, and n_0 and n are the initial and the current values of the porosity, respectively. This relationship was incorporated in the MPM code to simulate the same problem.

The solution for the settlement of the ground surface at time t is:

$$S_t = H_0(1 - exp(-m_{vl}q_u))\left(1 - \sum_{m=1}^{\infty}\frac{2}{M^2}exp(-M^2 T_v)\right) \tag{64}$$

Table 1
Material properties of 1D consolidation.

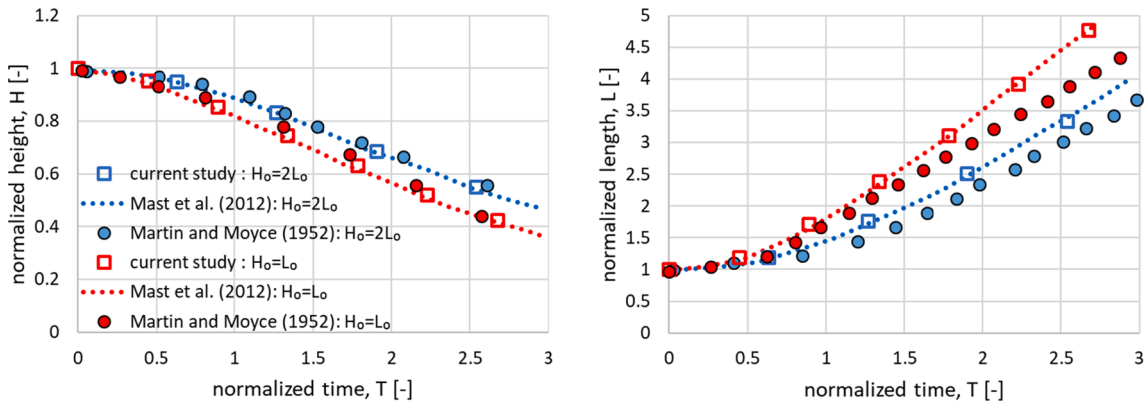| Material parameter	Description	Value
E	Young modulus	1000 kPa
ν	Poisson's ratio	0.0
n_0	Initial porosity	0.3
K_w	Bulk modulus of water	200×10^3 kPa
ρ_s	Density of solid grains	2650 kg/m^3
ρ_w	Density of water	1000 kg/m^3
k_0	Initial hydraulic conductivity	1×10^{-4} m/s

Fig. 2. Comparison between MPM simulations of the current study, experimental data for dam break analyses from Martin and Moyce (1952) and the numerical results of Mast et al (2012).
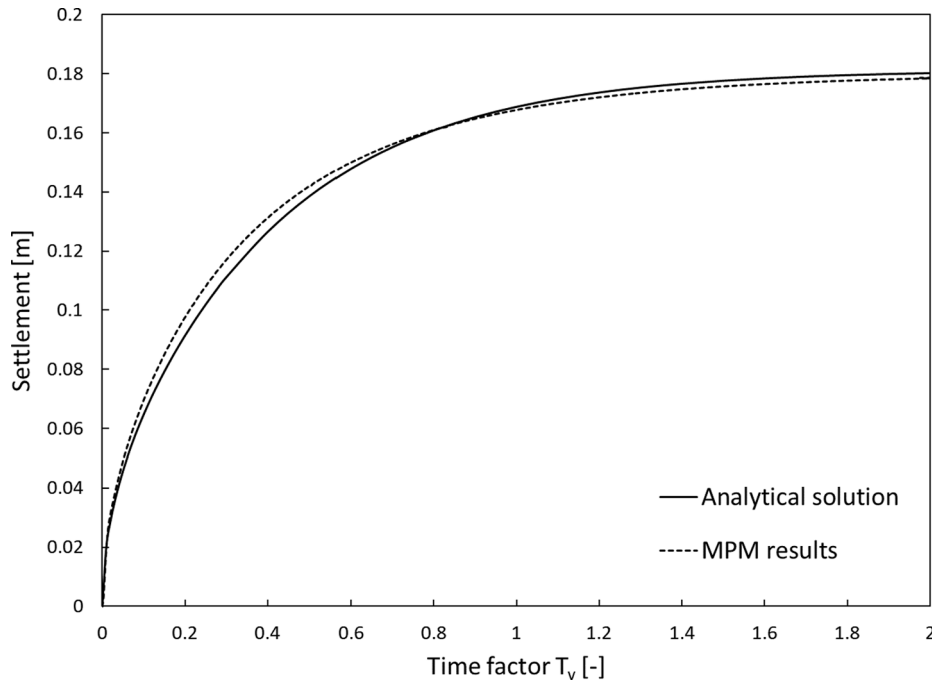
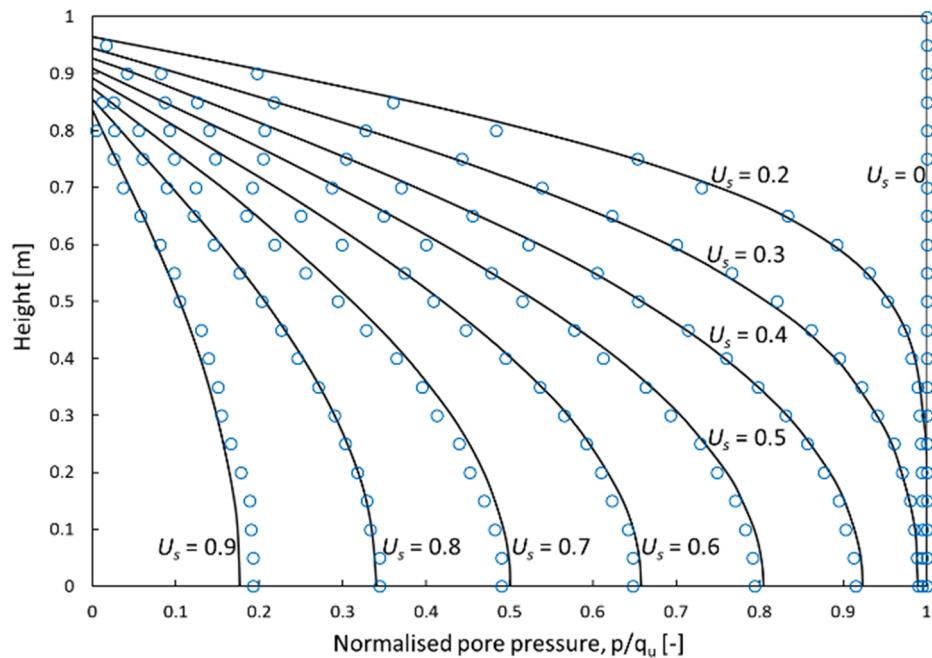**Fig. 3.** Analytical and numerical settlements of the soil column.

Fig. 4. Normalised pore pressure versus height; Solid lines: analytical solution; Dots: numerical results.

where

$$M = \left(m - \frac{1}{2}\right)\pi \tag{65}$$

and q_u is the external load, $m_{vl} = 1/E_{oed}$ is the coefficient of volume compressibility of the soil skeleton. E_{oed} is the oedometric stiffness. T_v is time factor defined as follows:

$$T_v = \frac{c_{v0}t}{H^2} \tag{66}$$

where H is the current height of the column and c_{v0} is the initial

coefficient of consolidation. When time tends to infinity, i.e. at complete consolidation, the ultimate settlement is:

$$S_\infty = H_0(1 - exp(-m_{vl}q_u)) \tag{67}$$

which corresponds to the deformation of an elastic drained soil layer in large deformation considering the logarithmic strain (Malvern, 1969), i. e. $\varepsilon = \ln(1 + S/H_0)$. The analytical solution of Xie and Leo (2004) was derived without considering Jaumann's objective stress rate of Kirchhoff stress. Therefore, the objective stress is not included in the current MPM simulation, i.e. the contributions of spin tensor and volumetric strain increment are neglected in Eq. (5).
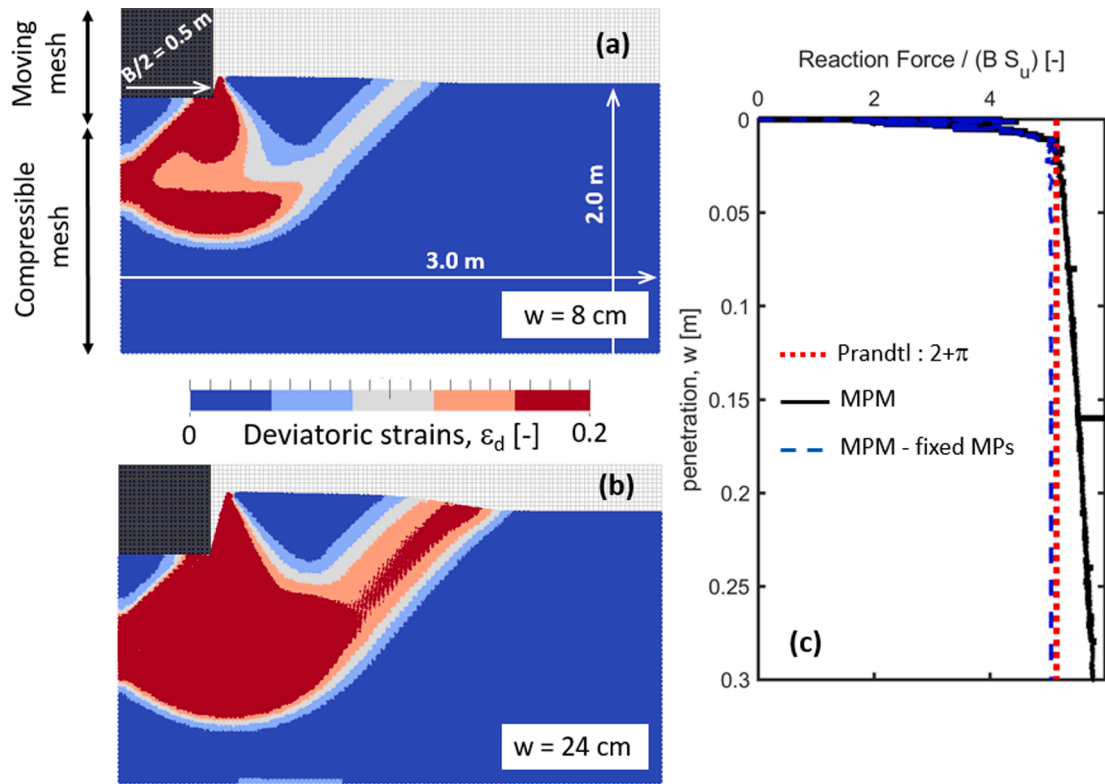
Fig. 5. Bearing capacity in undrained condition: (a) and (b) show the distribution of deviatoric strains after 8 cm and 24 cm of penetration respectively, (c) shows the load-penetration curves.

Fig. 3 shows the simulated settlement of the ground surface in time, which is in good agreement with the analytical solution of Xie and Leo (2004) over the entire range of T_v from 0 to 2.

The analytical solution of Xie and Leo (2004) also provides the distribution of the excess pore water pressures along the column as:

$$p = \frac{1}{m_{vl}} ln \left(1 + (exp(m_{vl}q_u) - 1) \sum_{m=1}^{\infty} \frac{2}{M} sin \left(\frac{Ma}{H_0} \right) exp(-M^2 T_v) \right) \quad (68)$$

where a is the depth of any point calculated from the ground surface.

Fig. 4 shows the distribution of the normalized pore pressures versus the height of the column for various average degrees of consolidation $U_s = S_t/S_\infty$. It can be seen that the MPM results compare very well with the analytical solutions.

3.3. Bearing capacity of a strip foundation

The penetration of a rigid strip foundation with a width B of 1 m is shown in Fig. 5. The foundation is pushed into a homogeneous clay layer with a thickness of 2 m. Due to the symmetry, half of the problem is modelled in the 2D plane strain condition. A width of 3 m is considered for the model, which is large enough to have negligible boundary effects. A fully rough boundary is used at the bottom of the domain whereas perfectly smooth conditions are applied to the lateral boundaries.

The clay is modeled as a single-phase material with a Tresca constitutive model. The density of the material, ρ, is 1990 kg/m³; the undrained cohesion s_u is 50 kPa; the shear modulus G is assumed to be 9 MPa, and the Poisson's ratio $ν$ is 0.495. Perfectly smooth contact is defined between the foundation and the soil. A structured computational mesh (4-node quadrilateral elements) is used with a uniform element size of 2.5 cm and 8 material points in each element. All material points of the foundation are moved with a constant velocity ($v = 2$ cm/s) to simulate the penetration. The moving mesh procedure (Al-Kafaji, 2013) is used to keep the contact surface on the same

computational nodes shared between the soil and the penetrating object, ensuring the highest accuracy in the results.

Fig. 5a and b shows the developed deviatoric strains after 8 and 24 cm of penetration, respectively. The shape of the failure mechanism is very similar to the one described by Prandtl (1920) for a frictionless material.

The normalized reaction forces are plotted in Fig. 5c. They are computed as the summation of all nodal forces along the contact surface and then divided by the factor ($B \cdot s_u$). The MPM simulation gives an increasing reaction force with depth, as the failure mechanism gets larger and the corresponding length of the shear planes increases. If the position of the material points is not updated (MPM – fixed MPs), the normalized reaction force reaches a vertical asymptotic value which is very close to the solution of Prandtl (1920), i.e. $2 + π$.

3.4. CPT in fine-grained soils

Schneider et al. (2007) published the experimental data of a series of undrained cone penetration tests (CPTu) in normally consolidated kaolin clay performed in centrifuge tests. The diameter of the piezocone is 10 mm and a conical tip with an angle of 60 degrees. The kaolin specimens were first consolidated in a pressing machine and then reconsolidated in the centrifuge. The material properties are summarized in Table 2.
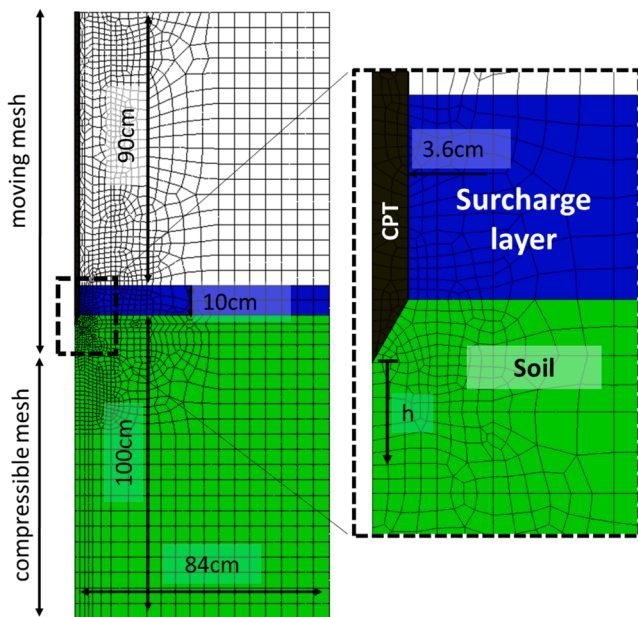
Table 2
Summary of the soil properties used for the kaolin clay (Schneider et al., 2007).

Parameter	Value	Description
G_s [–]	2.65	Specific gravity
n [–]	0.583	Initial porosity
λ [–]	0.26	Compression index
K [–]	0.06	Swelling index
φ′	23.5	Critical state friction angle

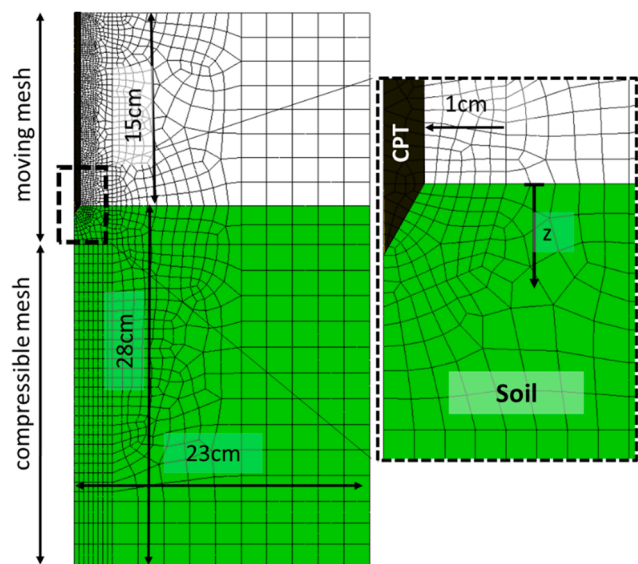**Fig. 6.** Geometry of the *1-g* numerical model.

Fig. 7. Geometry of the *160-g* numerical model.

The tests were performed by pushing the cone to a depth of about 100 mm at 160 g. The tests were repeated for different penetration velocity ranging from 0.0004 mm/s to 3 mm/s in order to obtain different drainage conditions: drained, partially drained, and undrained. The results of the tests are available in Schneider (2007). The data at 75, 85 and 95 mm of penetration were then used to determine the cone resistance at $\sigma'_{v0} = 80$, 90 and 100 kPa, respectively, as illustrated in Fig. 15.

Ceccato et al. (2016) modelled the experiments of Schneider (2007) using a 3D explicit MPM formulation in drained, undrained, and partially drained conditions. In this section, the same cone penetration tests are simulated using the proposed MPM formulation defined in 2D axisymmetric geometry (Galavi et al., 2018).

Two models are considered: a *1-g* and a *160-g* model. The *1-g* model is shown in Fig. 6 where the gravitational acceleration is $g = 9.81$ m/s^2. The geometry, boundary conditions and material point distribution are the same as the model in Martinelli and Galavi (2021). The diameter of the cone is 36 mm, which is larger than the one used in the experiment,
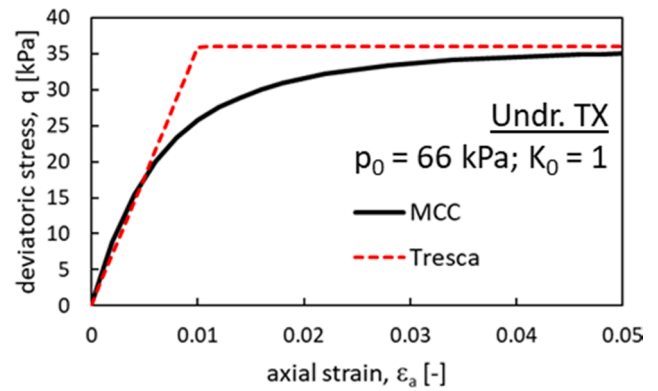

Fig. 8. Example of undrained triaxial test. Comparison between MCC and Tresca models.

Table 3
Summary of the parameters used in the Tresca model.

Parameter	Value	Description
G [kPa]	1000	Shear modulus
ν_u [–]	0.495	Undrained Poisson's ratio
s_u [kPa]	18.0	Undrained shear strength

but it is justified under the assumption that the results are independent of cone diameter (e.g. Lee and Salgado, 2005; Gavin, 2018). The correct initial vertical stress is applied by adjusting the unit weight of the surcharge layer. The node-to-node contact algorithm (see Section 2.1.2) is defined between the cone penetrometer and the surrounding soil. The *160-g* model is depicted in Fig. 7 where the gravitational acceleration is 160 g. Similar to the centrifuge experiment, the cone diameter is 10 mm in this model and the surcharge layer is not present.

In undrained and partially drained simulations, the bulk modulus of water is assumed to be 70 MPa, which is large enough to get an equivalent undrained Poisson's ratio ν_u higher than 0.495, as discussed in Ceccato et al. (2016).

Two constitutive models are used in this study: Modified Cam Clay (MCC) and Tresca. The MCC model is based on the Critical State concept and can properly simulate several aspects of the complex response of fine-grained materials: e.g. the nonlinear compressibility, hardening and stress-path dependence of the shear strength. The material parameters are summarized in Table 2 and the effective Poisson's ratio $\nu' = 0.25$.

The Tresca model was originally developed for metal plasticity, but it is widely used for failure analyses of normally consolidated clays. It is an elastic-perfectly plastic model using the Tresca failure criterion with constant stiffness and constant strength.

The mechanical responses of the MCC and Tresca models are compared in undrained triaxial test (Fig. 8). The confining stress is set to 66 kPa. The simulation with the MCC model shows a monotonic nonlinear behavior with the maximum deviatoric stress, q_{max}, of 35.8 kPa while the Tresca model gives a bilinear response. The material parameters of the Tresca model are listed in Table 3 which provide a good approximation of the MCC response. The shear modulus, G, of 1000 kPa is the secant shear modulus of the MCC model at 50% of q_{max} in q-ε curve.

3.4.1. Undrained response

In theoretical studies of the cone resistance in undrained clay, often elastic-perfectly plastic models such as Tresca or von Mises are used (e.g. van den Berg, 1994; Lu et al., 2004; Beuth and Vermeer, 2013; Qiu et al., 2011; Vesic, 1972, 1977; Teh and Houlsby, 1991). The cone resistance is commonly related to the undrained shear strength s_u through a cone factor N_c, defined as:
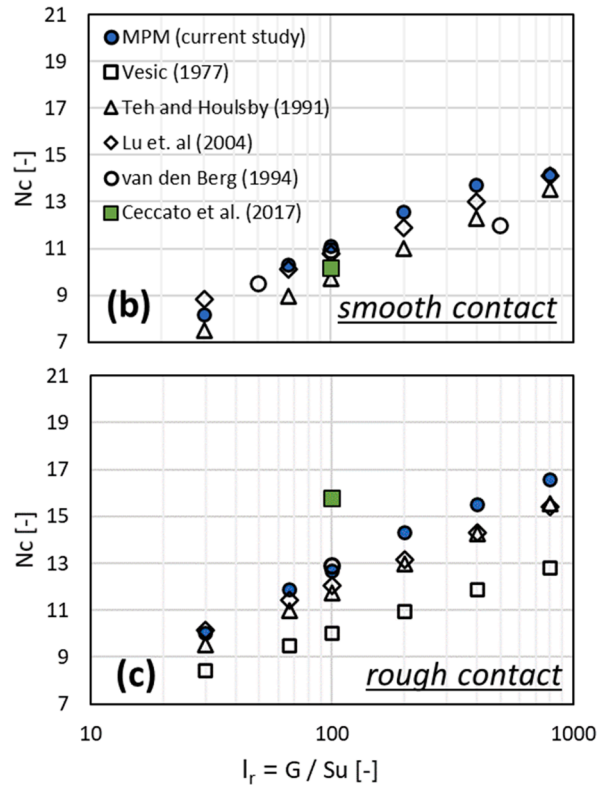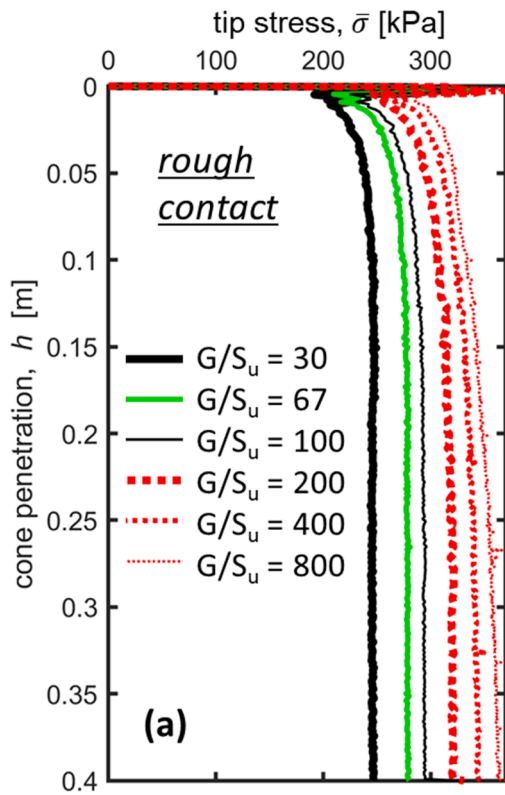
Fig. 9. Comparison between the MPM simulations and other studies using the Tresca model with shear strength $s_u = 18$ kPa. Effect of the rigidity index I_r and cone roughness.

$$N_c = \frac{q_c - \sigma_{v0}}{s_u} \qquad (69)$$

where σ_{v0} is the initial in-situ total vertical stress. The theoretical solutions indicate that N_c increases with the cone roughness and the rigidity index ($I_r = G/s_u$). This is illustrated in Fig. 9b and Fig. 9c for smooth and rough cones, respectively. It should be noted that the initial effective stress is isotropic and equal to 66 kPa.

The simulated tip stress ($\bar{\sigma}$), Eq. (70), is plotted versus the rigidity index, I_r for a rough cone in Fig. 9a. The soil parameters are listed in Table 3.

$$\bar{\sigma} = \frac{\sum_{i=1}^{n_{cone}} \bar{f}_{i,v}^{BC}}{A} \qquad (70)$$

where $\bar{f}_{i,v}^{BC}$ is the vertical component of the total reaction forces (i.e. Eq. (36)) along the contact surface; n_{come} is the number of nodes along the cone, and A is the area of the penetrometer.

For a given I_r, the simulated tip stress ($\bar{\sigma}$) increases with the penetration (h) until a relatively constant value (steady-state) is reached. Here, the steady state is reached after 30 cm of penetration. Therefore, the cone resistance q_c is defined as the value of $\bar{\sigma}$ reached at $h = 40$ cm. It is worth mentioning that the initial increase in $\bar{\sigma}$ at the beginning of the simulation is caused by the dynamic effect of the corner node, which has a very large mass. The large mass at the corner node, shared between the cone and shaft (Fig. 6), is a consequence of the large density specified for the surcharge layer. Once the cone is pushed deeper into the soil, the corner node will be surrounded by the clay soil and $\bar{\sigma}$, and consequently q_c, are not affected by the density of the surcharge layer anymore.

The simulated cone factor N_c agrees very well with the theoretical studies (Fig. 9b and c), in particular with the study of Lu et al. (2004) that is based on large-displacement finite element analyses using the Tresca model. Ceccato et al. (2017) simulated the tests using the Tresca model with a rigidity index, I_r, of 100, in which various contact cohesion
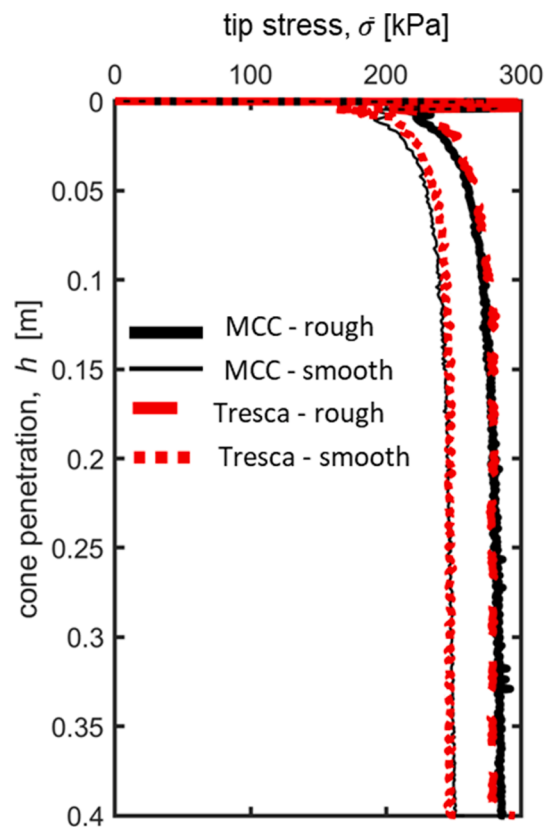

Fig. 10. Rough and smooth penetrometer. Comparison between the MCC and Tresca models in undrained condition.
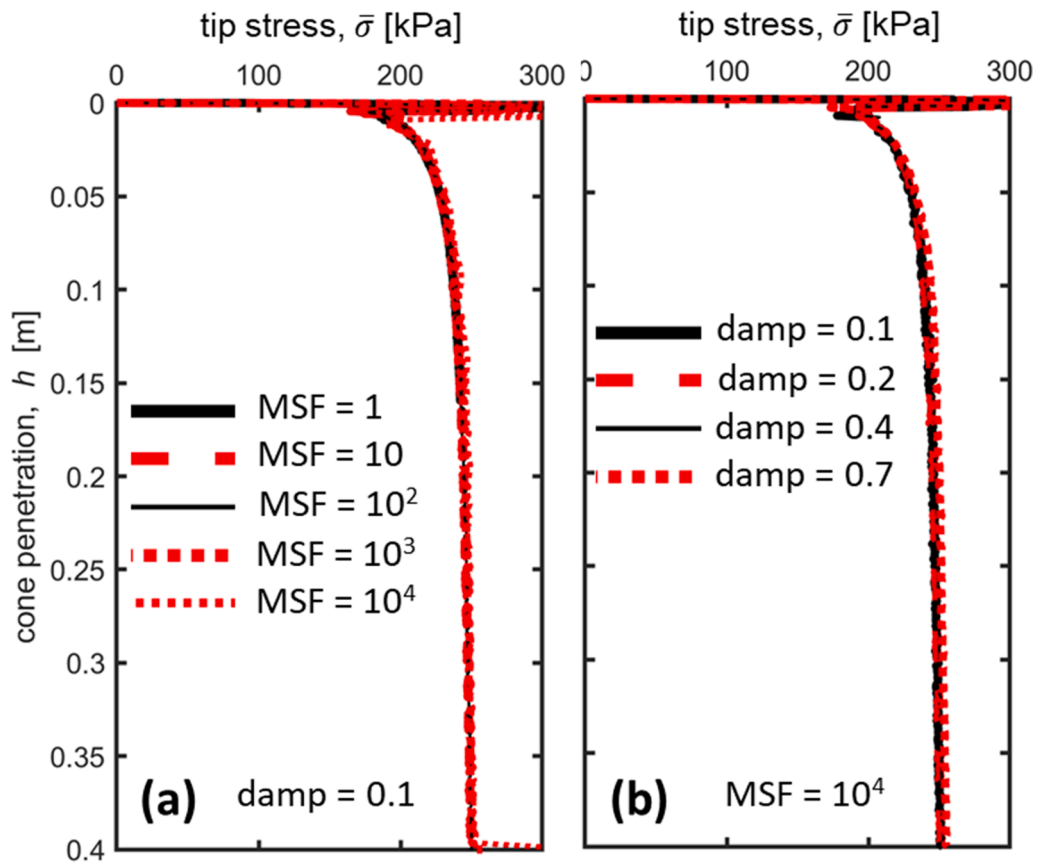
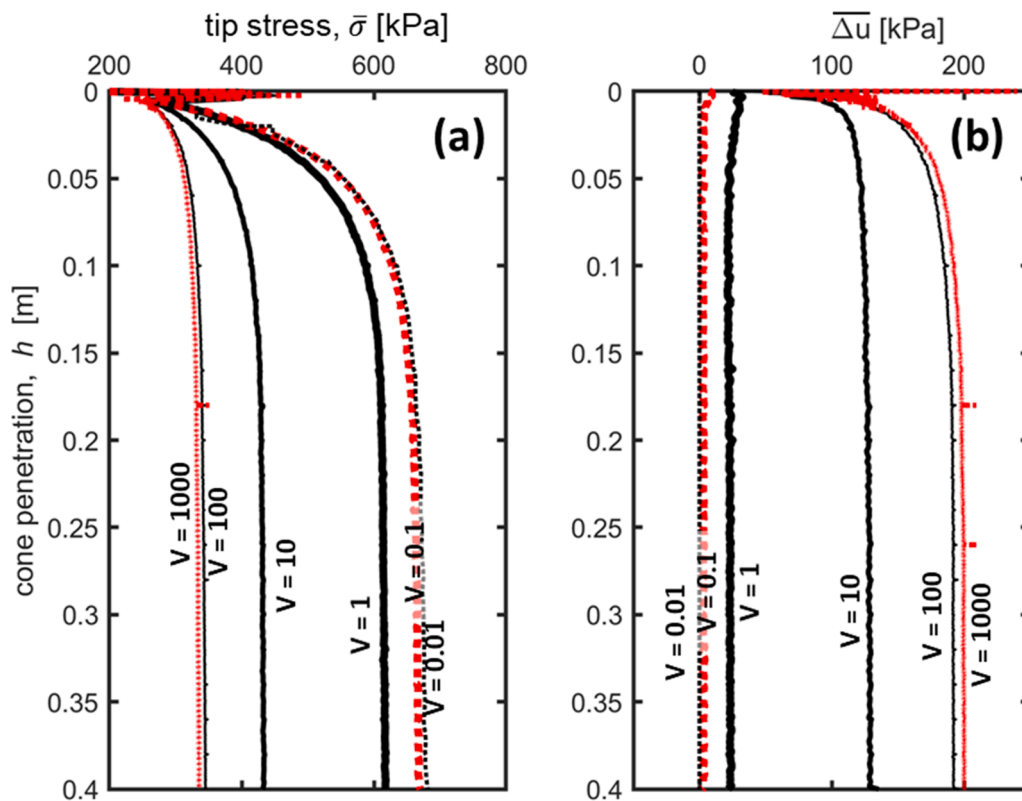**Fig. 11.** Sensitivity study. The MCC model with smooth contact. Effect of mass scaling and damping.

Fig. 12. MPM results of CPT penetration in kaolin clay: (a) tip stress and (b) average excess pore pressure as function of normalized penetration velocity V. Contact friction angle $\varphi_c = 15.6$ degrees.
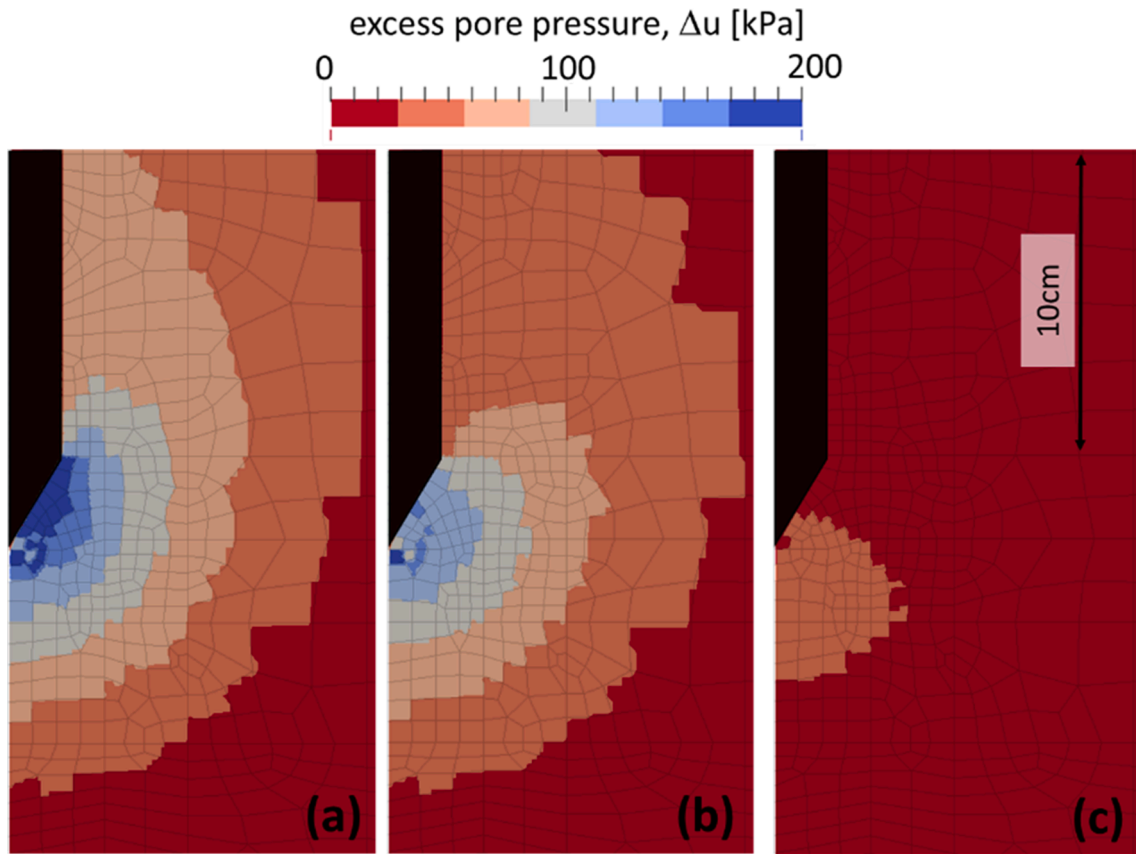
Fig. 13. distribution of Δu near the cone at $h = 40$ cm for: (a) V = 100; (b) V = 10; (c) V = 1.

were considered, ranging from a perfectly smooth to rough contact. As mentioned in Ceccato et al. (2017), the simulated cone factor N_c was slightly overestimated for non-smooth contacts. The source of the discrepancies was, however, not clear.

The undrained MPM simulation of the CPT is also performed using the MCC model, which is an effective stress model with the parameters listed in Table 2. The initial effective stress is isotropic and equal to 66 kPa. Although the two-phase formulation can also be used to simulate the undrained response, the more efficient one-phase undrained approach is adopted in this case (see Section 2.2). The MPM results (Fig. 10) show that the tip stresses $\overline{\sigma}$ computed with the MCC and Tresca models are nearly the same and agree well for both rough and smooth penetrometers.

The effect of mass scaling and damping factor is illustrated in Fig. 11 for the smooth penetrometer. Contrary to the findings of Ceccato et al. (2016) where high values of the damping factor led to an increase in the cone resistance, this study shows that $\overline{\sigma}$ is not significantly affected by the values of the damping factors. Similar findings were reported by Martinelli and Galavi (2021) for the simulation of CPT in dry sands.

3.4.2. Effect of partial drainage

The normalized penetration velocity (V), defined by Finnie and Randolph (1994), is used to compare CPT measurements with different penetration rate, cone diameters and consolidation properties:

$$V = \frac{v\mathrm{d}}{c_v} \tag{71}$$

where v is the cone penetration rate, which is conventionally 2 cm/s. d is the penetrometer diameter and c_v is the coefficient of consolidation. Randolph and Hope (2004) indicated that for normally consolidated kaolin, undrained conditions occur when V is larger than 30–100 and the fully drained conditions obtained when V is lower than 0.03–0.01. The

excess pore pressure becomes negligible if V is lower than 0.1.

The fully coupled MPM formulation (Section 2.1) is used here to show the effect of partial drainage during the penetration. The initial vertical and horizontal effective stresses are $\sigma'_{v0} = 90$ kPa and $\sigma'_{h0} = 54$ kPa, respectively. A friction angle of 15.6 degrees is considered along the contact between the soil and the penetrometer. To reduce the computational cost, similar to Ceccato et al. (2016), v is set to 2 cm/s and the variation of V is achieved by varying the hydraulic conductivity k, assuming it is constant and isotropic. The coefficient of consolidation is then calculated (Schneider et al., 2007) as:

$$c_v = \frac{k(1 + e_0)\sigma'_{v0}}{\lambda\gamma_w} \tag{72}$$

The numerical results are illustrated in Fig. 12 in which $\overline{\Delta u}$ is the average excess pore pressure at the cone, calculated as follows:

$$\overline{\Delta u} = \frac{\sum_{i=1}^{n_{cone}} \overline{f}^{BC}_{L,i,v}}{A} \tag{73}$$

where $\overline{f}^{BC}_{L,i,v}$ is the vertical component of the reaction forces of the liquid phase (i.e. Eq. (31)) along the contact surface. As expected, the cone resistance increases when V decreases. Overall, the numerical results confirm the findings of Randolph and Hope (2004), i.e. V = 100 and 1000 give nearly the same q_c, and the same holds for V = 0.1 and 0.01; a non-negligible $\overline{\Delta u}$ is also found when V is larger than 0.1.

The distribution of Δu is shown in Fig. 13 for different values of V. The undrained behaviour is observed for $V = 100$, where the Δu is about 200 kPa, and nearly drained behaviour at $V = 1$, where Δu is about 30 kPa. A partially drained condition is given for $V = 10$, where Δu has intermediate values between drained and undrained conditions.

The MPM results are compared against the experimental data in terms of normalized net cone resistance (Q) and normalized excess pore
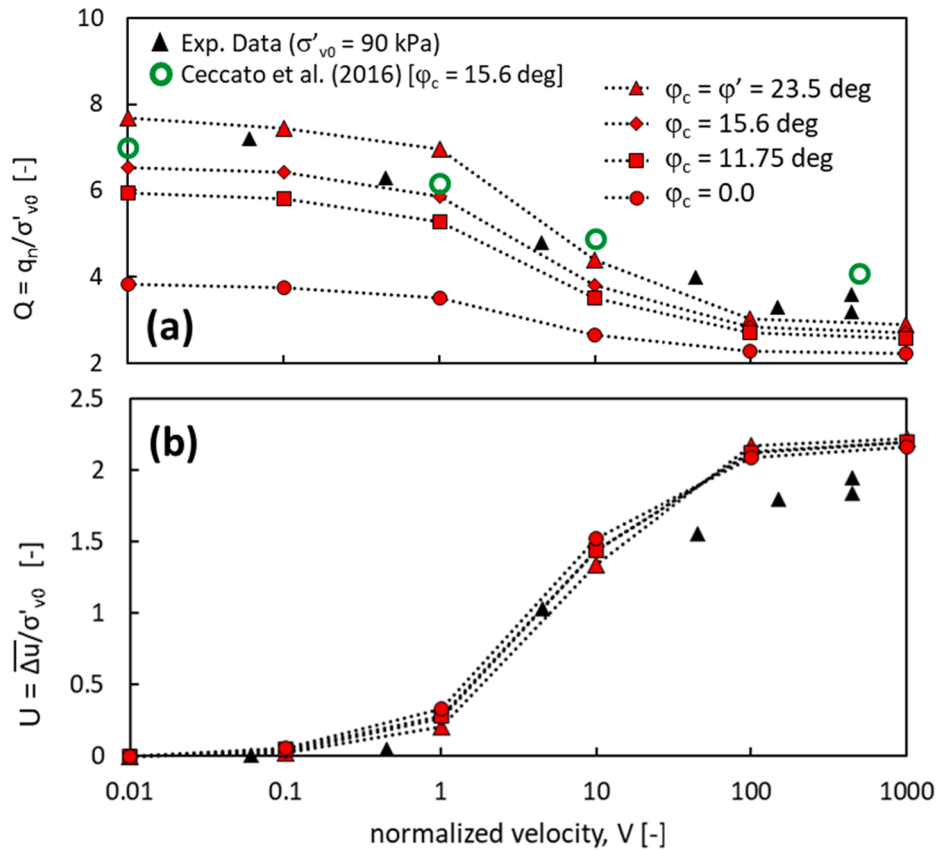
Fig. 14. comparison between MPM results and experimental data. Effect of the contact friction angle on (a) the normalized net cone resistance Q and on (b) the normalized excess pore pressure U.
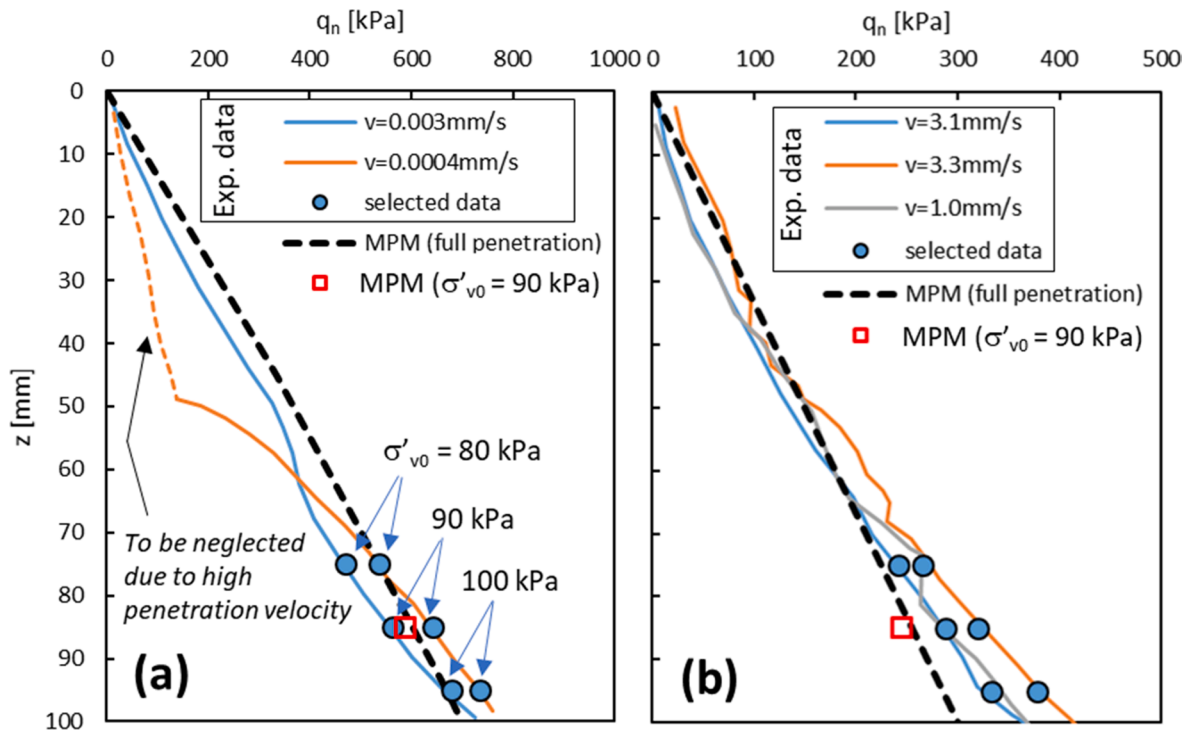

Fig. 15. comparison between the experimental and the numerical simulations at *160-g*: (a) drained and (b) undrained conditions. The continuous lines are the recording data from the centrifuge test. Blue circles: experimental q_n at σ'_{v0} = 80–100 kPa; Dashed lines: MPM simulations; Red square markers: simulated q_n with the *1-g* model at σ'_{v0} = 90 kPa (Fig. 6).
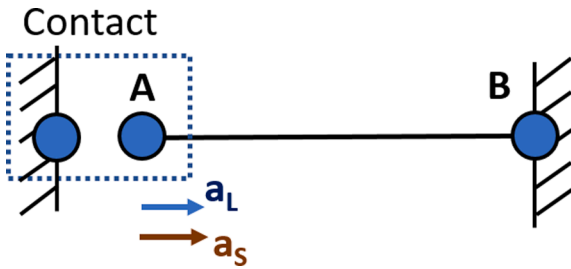
Fig. 16. 2-Node element with a contact node.

pressure (U) in Fig. 14. These variables are defined as follows:

$$Q = \frac{q_c - \sigma_{v0}}{\sigma'_{v0}} = \frac{q_n}{\sigma'_{v0}} \tag{74}$$

$$U = \frac{\overline{\Delta u}}{\sigma'_{v0}} \tag{75}$$

The results (Fig. 14) are shown for different values of contact friction angle φ_c. As expected, the value of Q strongly depends on the roughness of the cone, especially for the drained condition. Conversely, the value of U is almost independent of φ_c. For $V < 10$, the MPM results agree very well with the experimental data and with the results obtained numerically by Ceccato et al. (2016). For $V > 10$, the current study underestimates the experimental data, whereas Ceccato et al. (2016) overestimates it.

3.4.3. The 160-g MPM model

The results of the full penetration analysis at 160-g (Fig. 7), which represents the centrifuge test, are shown in Fig. 15 in terms of the net cone resistance q_n versus depth. The simulations are performed using the 1-phase (Section 2.2) and the coupled 2-phase formulations for the drained and (quasi) undrained conditions, respectively. To decrease the computational cost, the penetrometer is pushed with a velocity of 1 cm/s, and the hydraulic conductivity is set to 10^{-7} m/s to ensure an undrained response.

All MPM simulations exhibit a linear increase of q_n with depth. In the drained condition, the results agree very well with the experimental data over the entire penetration depth. Conversely, in the undrained conditions, all curves match for the first 70 mm of penetration. After that, the measured q_n is higher than the MPM results.

The apparent mismatch in the results of the undrained simulations (Fig. 14) is because the data points are selected at depths greater than 70 mm, where the numerical simulations deviate from the experiment. This can be seen in Fig. 15b. The reason for such deviation is unknown.

It is worth noticing that the value of q_n at z = 85 mm (i.e. σ'_{v0} = 90 kPa) is very close to the one computed with the *1-g* model (red square). This shows that the numerical results are independent of the numerical settings (e.g. model type, cone diameter, element size, etc.), highlighting the consistency and accuracy of the proposed MPM formulation.

4. Conclusions

This study presents an MPM formulation suitable for, but not restricted to, penetration problems. The numerical scheme can be used in combination with both structured and unstructured background meshes. Several enhancements have been made which are highlighted here:

- The use of 4-node quadrilateral elements in 2D geometries instead of 3-node ones. The 4-node element is preferred over the 3 node one, as it does not require nodal averaging to mitigate volumetric locking. Instead, the well-known B-bar method is adopted (Hughes, 2000). The proposed method can be directly extended to 3D problems using the 8-node hexahedral elements.
- A technique suitable to mitigate stress-oscillations is proposed for the 4-node quadrilateral elements, which is inspired from the Gauss integration method (Beuth, 2012; Al-Kafaji, 2013) widely used in Anura3D in triangular and tetrahedral elements. However, further investigations are necessary when this method is applied to the problems involving strain softening and localization. Therefore, at this moment, the method should be used with care if strain localization occurs.
- The critical review on how boundary conditions are applied in the computational scheme is thoroughly discussed. The new formulation is found to provide accurate contact forces, especially when high liquid pressures are present.

The proposed formulation is validated by simulating the water dam break, 1D large-strain consolidation, and strip footing bearing capacity problems. The results are in good agreement with the experimental data and the theoretical solutions.

Finally, cone penetration tests (CPT) in clay are simulated using two constitutive models, namely Tresca and Modified Cam Clay, which show that the numerical scheme is stable and accurate. The results are independent of the value of mass scaling and damping factor. The numerical model is then validated against the centrifuge test data of Schneider et al. (2007), where the MPM results match the experimental data over the entire range of drainage conditions.

CRediT authorship contribution statement

Mario Martinelli: Conceptualization, Methodology, Software, Validation, Writing – original draft. **Vahid Galavi:** Conceptualization, Methodology, Software, Validation, Writing – review & editing.

Declaration of Competing Interest

The authors declare that they have no known competing financial interests or personal relationships that could have appeared to influence the work reported in this paper.

Appendix

This section describes a validation example of the 2-phase coupled formulation (Section 2.1.3) when the contact is impermeable.

Fig. 16 shows a 2-node element. Node A is at the contact and node B is fully fixed. For the sake of simplicity, it is assumed that the mixture in the element has zero effective stress and non-zero liquid pressure. It is a 1D problem and the degrees of freedoms (DOFs) are $a_{L,A}$ and $a_{S,A}$ at node A. Neglecting the external and drag forces, Eq. (8) results in:

$$\overline{M}_{L,A} a_{L,A}^{t+1} = -\overline{f}_{L,A}^{int} \tag{76}$$

In case of impermeable contact, i.e. $a_{L,A}^{t+1}\big|_{afterF/C} = 0$, Eqs. (26) and (76) give:

$$\overline{f}_{L,A}^R = -\overline{M}_{L,A}a_{L,A}^{t+1} = \overline{f}_{L,A}^{int} \tag{77}$$

The corresponding rate of momentum of the solid phase (Eq. (13)) results:

$$M_{S,A}a_{S,A}^{t+1} = -f_A^{int} + f_{A,0}^R \tag{78}$$

where $f_{A,0}^R = \overline{f}_{L,A}^R$ since, at this step, contact formulation is only applied to the liquid phase.

The internal force of the mixture can be written as $f_A^{int} = f_A^{int}(\sigma') + \overline{f}_{L,A}^{int}$ where the first term is a function of the effective stress and the second one is a function of the liquid pressure. Since the effective stress is zero, $f_A^{int}(\sigma') = 0$, and $\overline{f}_{L,A}^{int} = \overline{f}_{L,A}^R$ (Eq. (77)). Therefore:

$$M_{S,A}a_{S,A}^{t+1} = -\overline{f}_{L,A}^{int} + \overline{f}_{L,A}^R = 0 \tag{79}$$

This means that the solid skeleton is already in equilibrium (i.e. $f_{S,A}^R = 0$), and the total reaction force at the contact is only function of the contribution of the liquid pressure ($f_A^R = \overline{f}_{L,A}^R$).

In contrast, if the rate of momentum of the solid phase is computed using the equation derived for the mixture, where all terms are evaluated before fixities or contact formulation (i.e. $f_A^R = 0$), it follows:

$$M_{S,A}a_{S,A}^{t+1} = -f_A^{int} - M_{L,A}a_{L,A}^{t+1} \tag{80}$$

and, using Eqs. (76) and (24), it becomes:

$$M_{S,A}a_{S,A}^{t+1} = -(1 - n_A)f_{L,A}^{int} \tag{81}$$

The rate of momentum of the solid phase is non-zero. It is proportional to the internal force in the liquid phase with opposite sign. If the pore pressure is positive (suction), then a gap is formed. Vice-versa, if the pore pressure is negative (compression), a non-realistic normal effective stress is calculated at the contact which results in a more severe soil-structure interaction.

The same result is obtained if the rate of momentum of the solid phase is computed using $M_{L,A}a_{L,A}^{t+1}\big|_{afterF/C}$ (which is zero after contact formulation) without considering the necessary reaction force term, i.e.:

$$M_{S,A}a_{S,A}^{t+1} = -f_A^{int} \tag{82}$$

References

Al-Kafaji, K.I., 2013. Formulation of a dynamic material point method (MPM) for geomechanical problems. PhD thesis. Univ. of Stuttgart, Germany.

Andersen, S., Andersen, L., 2009. Analysis of stress updates in the material-point method. Nordic Semin. Comput. Mech. 11, 129–134.

Arroyo, M., Butlanska, J., Gens, A., Calvetti, F., Jamiolkowski, M., 2011. Cone pentration tests in a virtual chamber. Géotechnique 61 (6), 525–531. https://doi.org/10.1680/geot.9.P.067.

Bardenhagen, S.G., Brackbill, J.U., Sulsky, D., 2000. The material-point method for granular materials. Comput. Methods Appl. Mech. Eng. 187, 529–541. https://doi.org/10.1016/S0045-7825(99)00338-2.

Bardenhagen, S.G., Kober, E.M., 2004. The generalized interpolation material point method. Comp. Model. Eng. Sci. 5 (6), 477–495.

Belytschko, T., Liu, W.K., Moran, B., Elkhodary, K., 2014. Nonlinear Finite Elements for Continua and Structures, 2nd Edition. Wiley. 2014. ISBN: 978-1-118-63270-3.

Beuth, L., Vermeer, P.A., 2013. Large deformation analysis of cone penetration testing in undrained clay. In: International conference on installation effects in geotechnical engineering (ICIEGE). Rotterdam. pp. 1–7. Taylor & Francis Group, London, ISBN 978-1-138-00041-4.

Beuth, L., 2012. Formulation and application of a quasi-static Material Point Method. PhD dissertation. University of Stuttgart.

Ceccato, F., 2014. Study of large deformation geomechanical problems with the Material Point Method. Ph.D. thesis. University of Padua, Italy.

Ceccato, F., Beuth, L., Simonini, P., 2017. Adhesive contact algorithm for MPM and its application to the simulation of cone penetration in clay. Procedia Eng. 175, 182–188.

Ceccato, F., Beuth, L., Vermeer, P.A., Simonini, P., 2016. Two-phase Material Point Method applied to the study of cone penetration. Comput. Geotech. 80, 440–452. https://doi.org/10.1016/j.compgeo.2016.03.003.

Ceccato, F., Yerro, A., Martinelli, M., 2018. Modelling soil-water interaction with the material point method. Evaluation of single-point and double-point formulations. CRC Press, p. 351.

Courant, R., Friedrichs, K., Lewy, H., 1928. Über die partiellen Differenzengleichungen der mathematischen Physik. Mathematische annalen 100 (1), 32–74.

Detournay, C., Dzik, E., 2006. Nodal mixed discretization for tetrahedral elements. In: Proceedings of the 4th International FLAC symposium, Numerical Modeling in Geomechanics. Minnesota Itasca Consulting Group, Inc., No. 07-02.

Fallah, S., Gavin, K, Jalilvand, S., 2016. Numerical modelling of Cone Penetration Test in Clay using Coupled Eulerian Lagrangian Method. In: Proceedings of Civil Engineering Research in Ireland 2016: 29-30 August, Galway, Ireland.

Finnie, I.M.S., Randolph, M.F., 1994. Punch-through and liquefaction induced failure of shallow foundations on calcareous sediments. Proc. Int. Conf. on Behavior of Offshore Structures, BOSS '94, Boston, pp. 217–230.

Fan, S., Bienen, B., Randolph, M.F., 2018. Stability and efficiency studies in the numerical simulation of cone penetration in sand. Géotech. Lett. 8 (1), 13–18. https://doi.org/10.1680/jgele.17.00105.

Galavi, V., Beuth, L., Zuada Coelho, B., Tehrani, F.S., Holscher, P., Van Tol, F., 2017. Numerical simulation of pile installation in saturated sand using material point method. Procedia Eng. 175, 72–79. https://doi.org/10.1016/j.proeng.2017.01.027.

Galavi, V., Martinelli, M., Elkadi, A., Ghasemi, P., Thijssen, R., 2019. Numerical simulation of impact driven offshore monopiles using the material point method. In: Proceedings of the XVII ECSMGE 2019, Reykjavik, Island. 2019. doi: 10.32075/17ECSMGE-2019-0758.

Galavi, V., Tehrani, F.S., Martinelli, M., Elkadi, A.S., Luger, D., 2018. Axisymmetric formulation of the material point method for geotechnical engineering applications. In: Proc., of 9th NUMGE Porto, Portugal. CRC Press. doi: 10.1201/9781351003629-53.

Gan, Y., Sun, Z., Chen, Z., Zhang, X., Liu, Y., 2018. Enhancement of the material point method using B-spline basis functions. Int. J. Numer. Method Eng. 113 (3), 411–431.

Gavin, K., 2018. Use of CPT for the design of shallow and deep foundations on sand. Cone Penetration Testing, Eds: Hicks, Pisano and Peuchen, Delft, The Netherlands.

Gibson, R.E., England, G.L., Hussey, M.J.L., 1967. The theory of one dimensional consolidation of saturated clays: I. Finite non-linear consolidation of thin homogeneous layers. Geotechnique 2, 261–273.

Hamad, F., 2016. Formulation of the axisymmetric CPDI with application to pile driving in sand. Comput. Geotech. 74, 141–150.

Hughes, T.J.R., 2000. The Finite Element Method: Linear Static and Dynamic Finite Element Analysis. Prentice-Hall, Englewood Cliffs, NJ.

Itasca, 2016. FLAC – Fast Lagrangian analysis of continua, version 8.0. Itasca Consulting Group, Minneapolis, MN.

Jassim, I., Stolle, D., Vermeer, P., 2013. Two-phase dynamic analysis by material point method. Int. J. Numer. Anal. Methods Geomech. 37 (15), 2502–2522. https://doi.org/10.1002/nag.2146.

Ji, W., Waas, A.M., Bazant, Z.P., 2010. Errors Caused by Non-Work-Conjugate Stress and Strain Measures and Necessary Correlations in Finite Element Programs. J. Appl. Mech. 77 https://doi.org/10.1115/1.4000916.

Kulak, R.F., Bojanowski, C., 2011. Modeling of Cone Penetration Test Using SPH and MM-ALE Approaches. In: 8th European LS-DYNA Users Conference, Strasbourg – May 2011.

Lee, J., Salgado, R., 2005. Estimation of Bearing Capacity of Circular Footings on Sands Based on Cone Penetration Test. J. Geotech. Geoenviron. Eng., ASCE 131 (4), 442–452.

Lu, Q., Hu, Y., Randolph, M.F., Bugarski, I.C., 2004. A numerical study of cone penetration in clay. Géotechnique 54, 257–267. https://doi.org/10.1680/geot.2004.54.4.257.

Malvern, L.E., 1969. Introduction to the Mechanics of a Continuous Medium. Prentice Hall, Englewood Cliffs, N.J.

Martin, J., Moyce, W., 1952. Part IV: An experimental study of the collapse of liquid columns on a rigid horizontal plane. Phil. Trans. Roy. Soc. Lond. 244, 312–324.

Martinelli, M., Galavi, V., 2021. Investigation of the Material Point Method in the simulation of Cone Penetration Tests in dry sand. Comput. Geotech. 130.

Martinelli, M., Alderlieste, E., Luger, D., Galavi, V., 2020. Numerical simulation of suction buckets using MPM. ISFOG 2020, Texas.

Mast, C.M., Mackenzie-Helnwein, P., Arduino, P., Miller, G.R., Shin, W., 2012. Mitigating kinematic locking in the material point method. J. Comput. Phys. 231 (16), 5351–5373. https://doi.org/10.1016/j.jcp.2012.04.032.

Mieremet, M., Stolle, D., Ceccato, F., Vuik, C., 2016. Numerical stability for modelling of dynamic two-phase interaction. Int. J. Numer. Anal. Meth. Geomech. 40 (9), 1284–1294.

Moormann, Ch., Sujith, G., Hamad, F., 2017. Simulation of offshore piling using advanced dynamic material point method (MPM). In: DFI-India 2017: 7th Conference on Deep Foundation Technologies for Infrastructure Development, Chennai, India, pp. 146–155.

Monforte, L., Arroyo, M., Carbonell, J.M., Gens, A., 2017. Numerical simulation of undrained insertion problems in geotechnical engineering with the Particle Finite Element Method (PFEM). Comput. Geotech. 82, 144–156. https://doi.org/10.1016/j.compgeo.2016.08.013.

Monforte, L., Arroyo, M., Carbonell, J.M., Gens, A., 2018. Coupled effective stress analysis of insertion problems in geotechnics with the Particle Finite Element Method. Comput. Geotech. 101, 114–129. https://doi.org/10.1016/j.compgeo.2018.04.002.

Phuong, N.T.V., Van Tol, A.F., Elkadi, A., Rohe, A., 2016. Numerical investigation of pile installation effects in sand using material point method. Comput. Geotech. 73, 58–71. https://doi.org/10.1016/j.compgeo.2015.11.012.

Prandtl, L., 1920. "Über die Härteplastischer Körper." Nachr. Ges.Wiss. Goettingen. Math.-Phys.Kl., pp. 74–85.

Qiu, G., Henke, S., Grabe, J., 2011. Application of a Coupled Eulerian-Lagrangian approach on geomechanical problems involving large deformations. Comput. Geotech. 38, 30–39. https://doi.org/10.1016/j.compgeo.2010.09.002.

Randolph, M.F., Hope, S., 2004. Effect of cone velocity on cone resistance and excess pore pressures. In; Proc. IS Isaka-Engineering Practice Performance Soft Deposits, Osaka, Japan, pp. 147–158.

Sadeghirad, A., Brannon, R.M., Burghardt, J., 2011. A convected particle domain interpolation technique to extend applicability of the material point method for problems involving massive deformations. Int. J. Numer. Meth. Eng. 86 (12), 1435–1456.

Schneider, J.A., Lehane, B.M., Schnaid, F., 2007. Velocity effects on piezocone measurements in normally and over consolidated clays. Int. J. Phys. Modell. Geotech. 7 (2), 23–34. https://doi.org/10.1680/ijpmg.2007.070202.

Schneider, J.A., 2007. Analysis of piezocone data for displacement pile design. PhD thesis. The University of Western Australia.

Spiezia, N., Ceccato, F., Salomoni, V., Simonini, P., 2015. Simulation of consolidation in large strains: A comparison between Finite Element Method and Material Point Method. In: Proc. VI International Conference on Computational Methods for Coupled Problems in Science and Engineering, COUPLED PROBLEMES 2015.

Stapelfeldt, M., Bienen, B., Grabe, J., 2021. Insights into Suction Caisson Installation Utilising the Material Point Method. In: Proc. International Conference of the International Association for Computer Methods and Advances in Geomechanics, pp. 802–809.

Staubach, P., Machac, J., Skowronek, J., Wichtmann, T., 2021. Vibratory pile driving in water-saturated sand: Back-analysis of model tests using a hydro-mechanically coupled CEL method. Soils Found. 61, 144–159. https://doi.org/10.1016/j.sandf.2020.11.005.

Stefen, M., Kirby, R.M., Berzins, M., 2008. Analysis and reduction of quadrature errors in the material point method (MPM). Int. J. Numer. Meth. Eng. 76 (6), 922–948.

Stolle, D., Jassim, I., Vermeer, P.A., 2010. Simulation of Incompressible Problems in Geomechanics. Comput. Methods Mech. 347–361.

Sulsky, D., Chen, Z., Schreyer, H.L., 1994. A particle method for history-dependent materials. Comput. Meths. Appl. Mech. Engrg. 118, 179–196. https://doi.org/10.1016/0045-7825(94)90112-0.

Teh, C., Houlsby, G., 1991. An analytical study of the cone penetration test in clay. Geotechnique 529–532. https://doi.org/10.1016/0148-9062(91)91308-E.

High-order, T.R.P.W.M., 2016. Material Point Method. MSc thesis. Delft University Press.

Tolooiyan, A., Gavin, K., 2011. Modelling the Cone Penetration Test in sand using Cavity Expansion and Arbitrary Lagrangian Eulerian Finite Element Methods. Comput. Geotech. 38 (4), 482–490. https://doi.org/10.1016/j.compgeo.2011.02.012.

van den Berg, P., 1994. Analysis of soil penetration. PhD thesis. Delft University Press.

Vesic, A.S., 1972. Expansion of cavities in infinite soil mass. ASCE J. Soil Mech. Found. Div. 98, 265–290.

Vesic, A.S., 1977. Design of pile foundations. Nat. Cooperation Hwy. Res. Program Rep. No. 42, Transportation Research Board, Washington, D.C.

Xie, K., Leo, C.J., 2004. Analytical solutions of one-dimensional large strain consolidation ofsaturated and homogeneous clays. Comput. Geotech. https://doi.org/10.1016/J.COMPGEO.2004.02.006.

Zambrano, L., Yerro, A., 2020. Numerical simulation of a free fall penetrometer deployment using the material point method. Soils Found. https://doi.org/10.1016/j.sandf.2020.04.002.

Zhang, D.Z., Ma, X., Giguere, P.T., 2011. Material point method enhanced by modified gradient of shape function. J. Comput. Phys. 230 (16), 6379–6398.

Zheng, X., Pisanò, F., Vardon, P.J., Hicks, M.A., 2021. An explicit stabilised material point method for coupled hydromechanical problems in two-phase porous media. Comput. Geotech. 135, 104–112.